IEEE Access
Multidisciplinary | Rapid Review | Open Access Journal

Received January 30, 2016, accepted February 21, 2016, date of publication March 31, 2016, date of current version April 6, 2016.

Digital Object Identifier 10.1109/ACCESS.2016.2542478

Millimeter Wave Networked Wearables in Dense Indoor Environments

KIRAN VENUGOPAL, (Student Member, IEEE), AND ROBERT W. HEATH, JR., (Fellow, IEEE)
The University of Texas, Austin, TX 78712, USA

Corresponding author: K. Venugopal (kiranv@utexas.edu)

This work was supported in part by the Intel-Verizon 5G Research Program and by the National Science Foundation under Grant No. NSF-CCF-1319556.

ABSTRACT Supporting high data rate wireless connectivity among wearable devices in a dense indoor environment is challenging. This is primarily due to bandwidth scarcity when many users operate multiple devices simultaneously. The millimeter-wave (mmWave) band has the potential to address this bottleneck, thanks to more spectrum and less interference because of signal blockage at these frequencies. In this paper, we explain the potential and challenges associated with using mmWave for wearable networks. To provide a means for concrete analysis, we present a system model that admits easy analysis of dense, indoor mmWave wearable networks. We evaluate the performance of the system while considering the unique propagation features at mmWave frequencies, such as human body blockages and reflections from walls. One conclusion is that the non-isotropy of the surroundings relative to a reference user causes variations in system performance depending on the user location, body orientation, and density of the network. The impact of using antenna arrays is quantified through analytic closed-form expressions that incorporate antenna gain and directivity. It is shown that using directional antennas, positioning the transceiver devices appropriately, and orienting the human user body in certain directions depending on the user location result in gigabits-per-second achievable ergodic rates for mmWave wearable networks.

INDEX TERMS Millimeter wave communication, personal communication networks, indoor communication, internet of things, wearable computers, virtual reality, signal to noise ratio, analytic models, performance analysis.

I. INTRODUCTION TO WEARABLE NETWORKS

Mobile wearable computing devices are rapidly making inroads due to advancements in miniature electronics fabrication technology, mobile wireless communication, efficient batteries, and increasingly capable data analytics. The major driver of the mobile electronics market has been fitness and health-care gadgets [1], [2]. These low-end devices typically require long battery life and only require lower data rate connections to other devices. Recently, a new class of high-end wearable devices is emerging with relaxed power constraints and high data rate requirements.

There are several examples of high-end wearables, such as smartwatches, augmented reality glasses, accurate navigation assists, and virtual reality helmets/goggles. The applications involved may make use of high data rates, and the devices may be charged daily. While these devices could have their own cellular connection, it seems likely that they will instead form a network with the smartphone as a hub, creating a *wearable network*. An illustration of a wearable network is shown in Fig. 1. A coordinating on-body hub like the smartphone can ensure that interference from wireless devices attached on a given user's body is minimized. Further, smartphone has larger computing power than the other devices in the wearable network and is usually connected to wireless hotspots and/or cellular network. Hence smartphones can act as aggregating nodes to process various sensor data inputs as well as host multimedia contents for infotainment applications in wearable displays.

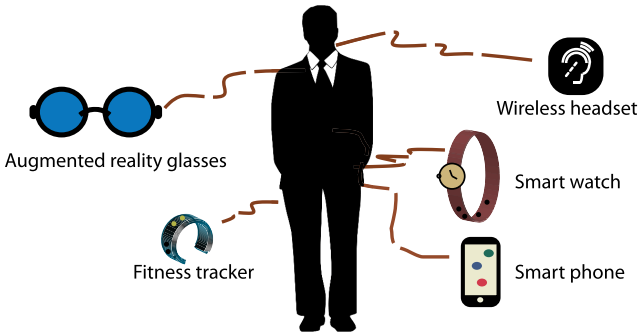

FIGURE 1. Figure showing several mobile wearable devices attached around a user's body. These devices form a wireless network around the user and is termed a wearable network.

Most work on Body Area Networks (BANs) has focused on low-end devices, especially in man-to-machine communication and health-care [3], [4]. These short-range wireless networks consist of body-surface-mounted electronic devices or in-body implants that transmit data to an on-body or off-body gateway device [5]. The IEEE 802.15.6 standard for the wireless BAN aims to provide low power and highly reliable wireless communication for BANs supporting data rates up to 10 Mbps [6]. These technologies are not feasible for high-end applications like uncompressed video streaming or augmented reality in wearable networks because of the rate requirements of the order of Gbps and the potential for very low latency. Note that the range of operation is not a major concern for these high-end devices in a wearable network, with device-to-device wireless link lengths usually less than a meter.

Using millimeter wave (mmWave) communication is one approach to provide high data rates in wearable networks [7], [8]. The mmWave frequency bands have large bandwidth, good isolation, and better co-existence due to directional antennas. WirelessHD [9] released in 2008 offers multi-gigabit wireless connectivity specifications for the 60 GHz unlicensed mmWave band to support high-definition video and audio digital transmission to replace wired interconnects. Following WirelessHD, IEEE 802.11ad [10] was released and offered several use cases for short range communication systems also at 60 GHz. These standards and other mmWave-based standards like the ECMA-387 and the IEEE 802.15.3c do not explicitly incorporate wearable networks as a use case. The Task Group ay for IEEE 802.11 is now considering mmWave-based high-end wearables in public places as a possible use case. As a consequence, industry is recognizing the importance of millimeter wave for high-end wearables.

Crowded indoor environments are perhaps the most challenging for wearable networks due to high interference caused by the simultaneous operation of wearable devices by several users within close proximity. A typical example of a dense environment is a commuter train or other public transportation systems during rush hour as shown in Fig. 2, where the user density could be as high as three users per square meter [11]. In conventional wireless BANs, this is not a major issue as the data-rate requirements are much lower. For high-end devices in a wearable network, coordination across users could reduce interference. But this would increase the overhead data and may add to the complexity and cost of the devices [12]. Abrupt change in the high crowd density may also be detrimental to the existing connections. A desirable feature of a wearable network, thus, is to support intra-network communication between devices in a way that is independent of other users' wearable networks. The mmWave signals are blocked by human body and objects, and hence the mmWave band is an ideal candidate to deliver high data rates in wireless personal area networks [8]. This is promising for dense deployments of wearable networks involving simultaneous operation of many devices [12], [13].

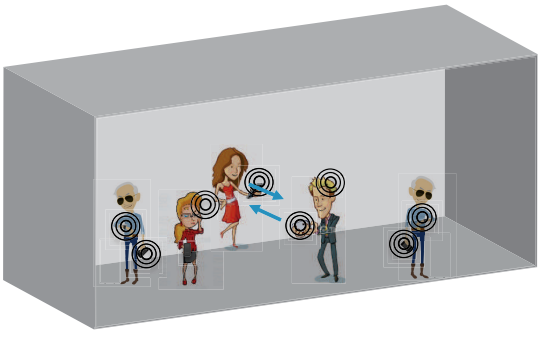

FIGURE 2. Figure illustrating a typical crowded indoor scenario such as a train car with several users operating their respective wearable networks.

There is limited prior work related to mmWave wearable networking. A comparison between body area networks at 2.5 GHz and 60 GHz in terms of inter-network interference in indoor environment using CAD model and simulation was reported in [13]. Their study concluded that significant amount of interference mitigation can be achieved by using the mmWave band, allowing a greater number of collocated wearable networks. Prior work in [12] used ray tracing tool to show that the use of mmWave is critical to support massive deployment of wearable networks with high-end devices in indoor commuter train scenario. It was also noted that the existing mmWave technologies have to be enhanced to efficiently handle the scenarios where several neighboring users' networks overlap. In [14], the effect of first order reflections for mmWave signal propagation in indoor operations of wearable networks was characterized and system performances when a user is located at the center and a corner of an indoor enclosure were evaluated using simulations.

In this paper, we present a system model to study the feasibility of mmWave wearable networks in the absence of coordination across the users. The model can be used to evaluate the worst case performance of a mmWave-based indoor single-hop communication system when crowd density is high and in the absence of an advanced medium access (MAC) protocol. We incorporate the effect of user density and orientation of the user body relative to the wearable devices in the model to understand the best conditions for achieving maximum system performance. Using directional antennas in the wearable devices, and assuming the users are randomly located in the indoor environment, we analyze performance of a typical user's on-body mmWave communication link. Using the analytic results, we show how system performance is non-isotropic in an indoor environment and varies as a function of both location as well as body orientation of the reference user.

The rest of the paper is organized as follows: In Section II, we highlight the challenges of using mmWave communication in diverse areas including circuits, antennas, propagation, and performance analysis. In Section III, we first review key prior work related to modeling wireless networks and then proceed to explain the proposed system model. This is

followed by the derivation of spatially averaged signal-to-noise-plus-interference-ratio (SINR) distribution in Section IV which leads to closed-form expressions for system performance. In Section V, we provide simulation results to validate the analysis done in Section IV. We summarize the main results of the paper in Section VI. Finally, the detailed proofs of Lemmas and Theorems stated in Section IV are provided in Appendices.

II. CHALLENGES OF COMMUNICATING USING mmWAVE IN WEARABLE DEVICES

A. HEALTH CONCERNS

Before mmWave devices are introduced in the consumer market of wearables, their compliance to radiation exposure guidelines as set out by the government has to be ensured. The sensitivity of human eye tissues and skin to mmWave frequencies needs to be analyzed more carefully before large scale deployment of mmWave devices, because high-intensity direct exposure of mmWave frequencies could cause ocular injury.

The preferred metric to determine compliance for devices operating at higher carrier frequencies is power density rather than specific absorption rate [15]. Given that the wearable devices would be held close to the body, reliable power density measurements are hard to obtain since the resulting electromagnetic fields are near-field. For distances less than 5 cm between devices and the human body, analytic tools may be used to compute power density numerically. Temperature elevation measurements are yet another way to evaluate compliance on mmWave devices [16], [17]. It was noted in [16] that longer, low-intensity exposure to mmWave signals, for example, 10 mW/cm^2 for upto 8 hours, appears to be safe.

B. CIRCUITS

The higher carrier frequencies and higher bandwidths pose several challenges for the design of RF circuits, mixed signal components, and the digital baseband. The high dielectric constant of most of the semi-conductors used today can result in a dielectric waveguiding effect depending on the size of the substrate. This could lead to energy loss for chip components or energy radiation in undesired directions [18] at mmWave frequencies. The leaked energy could even result in parasitic coupling between on-chip components. This poses problems for modeling transistors and passive devices, and requires careful treatment of small parasitic components within the model.

Another design challenge is to develop linear RF power amplifier which is a key ingredient to meet link budget of mmWave systems. These power amplifiers would need to operate at low-voltage supplies of the current semi-conductor technology while providing large dynamic ranges required for certain modulations [19].

The analog-to-digital converters (ADcs) can be a significant source of power consumption due to the wide bandwidth of the signals that need to be sampled. The issue is compounded with the use of many antennas. Potential solutions including analog, hybrid analog/digital, and low resolution ADCs are described in the next section. Commercial products based on mmWave systems such as the IEEE 802.11ad and WirelessHD are already available in the market today in high volume consumer applications. Hence, significant progress is being made on addressing these challenges.

C. ANTENNAS

Multiple antennas are widely used in mmWave communication systems to obtain array gain. Different antenna array configurations have been suggested in the literature in part to overcome other power constraints. Analog beamforming is normally implemented as a phased array where signals from different antennas are co-phased by digitally controlled phase shifters and combined in the RF circuits [20]. For example, Wilocity has products with 32 antenna elements that are arranged in an almost omni-directional fashion to improve performance [21]. Hybrid digital and analog precoding or combining uses multiple banks of analog phase shifters to obtain some of the leverages of MIMO communication [22]. Switches may be used instead of phase shifters [23] to reduce hardware complexity and power consumption. Lens antennas can also be used for transceiver complexity reduction though the size may be prohibitive for the wearable scenario [24].

Due to feed-line losses, antenna arrays need to be placed in close proximity to the RF circuits. While in-package and on-chip antennas [25] are both potential solutions, multiple arrays may be required on a device surface to avoid blockage due to fingers [26]. This will complicate the distribute of feeding of antennas on wearables.

In our work, we will consider wearable devices with a single array that uses analog beamforming to steer the transmit and receive beams. Omni-directional antennas will be a special case.

D. PROPAGATION

MmWave propagation in the 60 GHz band is well understood, due to past work for IEEE 802.15.3c [27] and IEEE 802.11ad [10]. Most work though was done with different use cases in mind, especially in cable replacement.

Blockage is a significant issue for mmWave in general, and specifically for wearable networks. The inadvertent movement the user's hands, for example, could occlude the on-body transmitter - receiver direct signal link in a wearable network. The blockage of signal due to the placement of fingers over the antenna arrays is yet another modeling challenge. The accurate variation in the propagation environment is difficult to model without detailed measurement data for such cases. Both ray-tracing and measurement-based studies have been used previously to study mmWave propagation in indoor environments [28]–[31]. These, however, do not include several number of human users in the measurement chamber.

The finite dimensions of the indoor environment also play a key role in the spatial non-isotropy of system

performance in indoor mmWave based wearable networks [12], [32]. Another important feature in indoor mmWave wireless systems is the predominant effect of signal reflections off the wall and ceilings [12], [14], [33]. This could potentially amplify the interference signals from another user's wearable network and thus degrade the SINR in a typical user's signal receiver. This important factor is elaborated further and is modeled in our analysis. In this paper, we will consider an indoor setup that has many users with wearable networks. We will consider the effects of wall and ceiling reflections in our models, as well as blocking effects of other people [34].

III. MODELING MMWAVE WEARABLE NETWORKS WITH STOCHASTIC GEOMETRY

Developing tractable models to characterize performance of mmWave-based wearable networks is key to understanding the impact of crowd density and the necessity of coordination across users via advanced protocols if the performance without inter-user coordination is poor. In this section, we elaborate on the analytic approach used in the paper to model wearable networks. The network geometry, blockage model and the propagation features assumed are explained and the intuitive reasoning for the assumptions made are provided at relevant places. The performance analysis and modeling leverage tools from stochastic geometry which is reviewed next.

A. BACKGROUND ON STOCHASTIC GEOMETRY

Stochastic geometry provides a mathematical approach for modeling wireless networks, which has been used to study outdoor systems. The transceiver nodes in the network are modeled as randomly located in the 2-D plane to form a point process of known intensity, and the distribution of the interference field as seen by a typical user is analyzed. Stochastic geometry allows derivation of analytic expressions for average performance metrics like the SINR, spectral efficiency, and the sum throughput for infinite networks [35]–[37].

In the context of mmWave-based cellular systems, [38], [39] used results from stochastic geometry to characterize network coverage and capacity. The important propagation features of the mmWave signal, especially signal blockage due to buildings and human user body were modeled in [39] and [40]. In [40], a distance-dependent blockage model was first derived using results from random shape theory, and was then used to derive analytic expressions for SINR coverage. An important assumption for these derivations was that the sources of signal blockages (buildings) and the communication devices are drawn from independent Poisson Point Processes (PPP).

For dense indoor operations using mmWave, human bodies of the users are the main source of blockages and can result in 30-60 dB of attenuation for mmWave signals [41]–[43]. The users that carry potentially interfering devices, hence, also potentially block the interference from other users. This is a key difference compared to outdoor cellular based mmWave systems where independent spatial distribution assumption for blockages and interferers is easier to justify. Another point of difference between outdoor cellular systems and indoor mmWave systems is the spatial extent and number of transceiver devices considered in the analysis. While an infinite region of operation and infinite number of users could be justified in a cellular setting, system models for indoor operation have to consider finite geometry and number of users.

Previous work in [32] considered the impact of non-isotropy in the environment and derived SINR coverage probability expressions when finite number of users are present within a finite region. Using the approaches in [40], [44], and [45], closed-form expression for spatially averaged performance seen by a typical user located at the center of a finite enclosure was derived in [34]. The main limitation in [32] and [34] is that the effect of wall and ceiling reflections in the metallic indoor environment was not explicitly modeled. The exact effects of first order reflections from all the six faces of a cuboidal enclosure were considered for the simulation results in [14]. This provided valuable insight into the nature of surface reflections in the indoor mmWave setup. While it was assumed that the reflections from the ceilings were never blocked and the self-body human blockage was characterized, [14] does not consider directional antennas at the devices and also does not report closed-form analytic expressions for spatially averaged system performance. The system model that we explain next leads to closed-form expressions for spatially averaged performance of a typical user's wearable network communication link.

B. NETWORK MODEL

To model a train car, we consider an enclosed space $\mathcal{T}$ of dimensions $L \times B \times H$ as shown in Fig. 3(a) which has highly reflective walls and ceiling, and a non-reflective floor. Such a model is similar to that used in [14], with the exception that we assume the floor to be non-reflecting as the material used for flooring is generally rougher, and different from the smooth surfaces of the walls and ceiling [46]. Note that seating arrangements and other finer details of the interior of a typical train car are neglected in this model. The users are assumed distributed randomly within $\mathcal{T}$ and are modeled as cylinders $\mathcal{U}$ of a fixed diameter W, ideally characterizing the width of the human body torso including the legs. Each user is assumed to be equipped with one high-end wearable receiver and one controlling hub (smartphone) which acts as the device-to-device communication transmitter.

All the mmWave wearable transmitter devices are assumed to be positioned at a depth d_{h} from the ceiling of $\mathcal{T}$ along the plane denoted as $\mathcal{P}$ (Fig. 3(a)) and positioned randomly on a circle of radius $d \geq W/2$ concentric with their associated user. Typical values for d can vary from 2-30 centimetres depending on whether the device is placed on the body surface or held on stretched hand. The interfering transmitters and their locations are denoted as $\mathsf{T}_i = x_i + \mathrm{j}y_i$. In this representation, the point $\mathcal{O}$ as shown in Fig. 3, is assumed

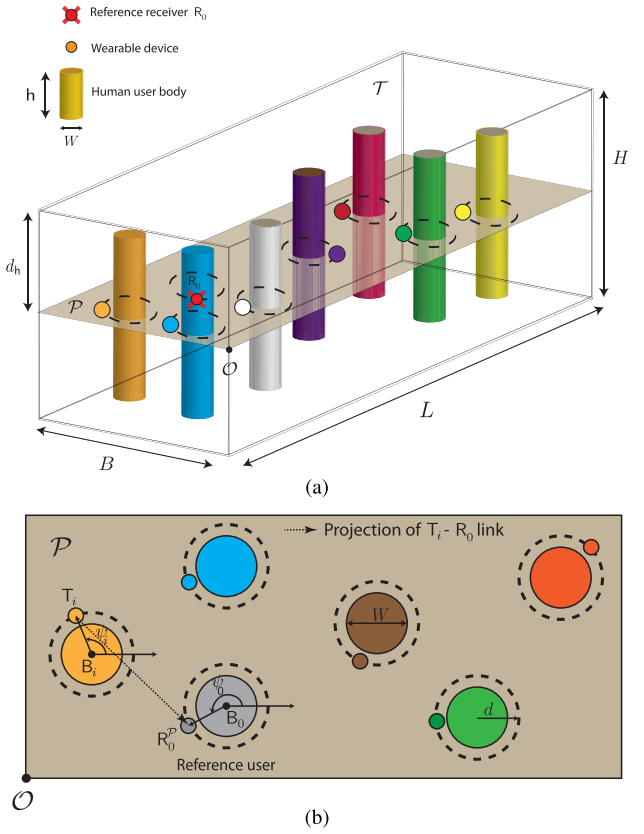

FIGURE 3. Network model showing the human users, reference receiver R_0, reference and interfering transmitters. All the wearable devices are at a distance d around the diameter-W user body. (a) 3-D model showing the enclosed region $\mathcal{T}$ and the wearable transmitters positioned in the plane $\mathcal{P}$. (b) 2-D model in $\mathcal{P}$ illustrating the user-body orientation representation used in this paper.

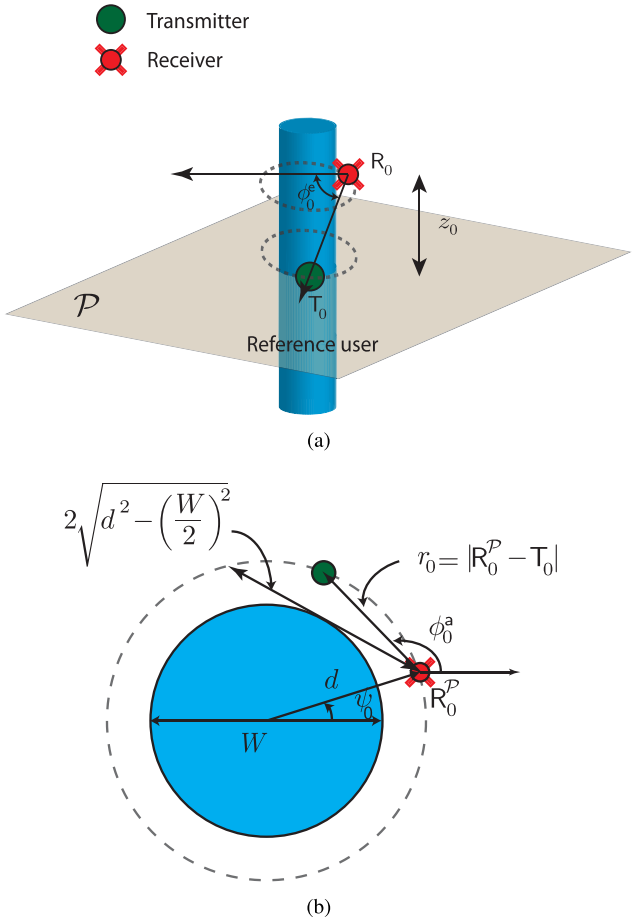

FIGURE 4. Illustration showing the reference signal link's geometry. (a) Reference signal link in 3D. The reference receiver is at a height z_0 above the reference transmitter and forms an elevation angle ϕ_0^e with the plane containing the transmitters $\mathcal{P}$. (b) Projection of the reference receiver onto $\mathcal{P}$ showing the azimuth angle ϕ_0^a between the reference user's devices and the horizontal separation r_0. The reference link is unblocked whenever (3) holds.

to be the origin. We denote the reference receiver and its location by R_0 which is also assumed to be at a distance d from the reference user's body. Further, the separation between R_0 and the reference transmitter T_0 is assumed to be r_0 in the azimuth and z_0 in the elevation plane. The geometry of the reference transmitter-receiver is illustrated in Fig. 4. The projection of the reference receiver onto $\mathcal{P}$, the plane containing the transmitters is denoted by the complex number $\mathsf{R}_0^{\mathcal{P}} = x_0 + \mathrm{j}y_0$, so that $|\mathsf{R}_0^{\mathcal{P}} - \mathsf{T}_0| = r_0$. We use the following notations (see Fig. 4) for the azimuth and elevation angles of the reference transmitter relative to the reference receiver.

$$\phi_0^{\mathsf{a}} = \measuredangle(\mathsf{T}_0 - \mathsf{R}_0^{\mathcal{P}}) \text{ and} \tag{1}$$

$$\phi_0^{\mathsf{e}} = -\arctan\left(\frac{z_0}{r_0}\right). \tag{2}$$

User bodies $\mathcal{U}$ intersect with $\mathcal{P}$ to form diameter-W disks. We use the notation B_i to denote both this disk as well as its center for the i^{th} user. We assume $\{\mathsf{B}_i\}$ are drawn from a non-homogeneous PPP Φ that has intensity λ in the region of interest, and zero outside it. This assumption eases analysis for mmWearable wearable networks in crowded environment [47] and also captures the uniform but random crowd distribution inside a public transportation system during rush hours. Since the transceivers are located relative to the users carrying them, we say user i is facing towards a direction $\psi_i = \measuredangle(\mathsf{T}_i - \mathsf{B}_i)$. The reference receiver R_0 is assumed to be facing towards the direction $\psi_0 = \measuredangle\left(\mathsf{R}_0^{\mathcal{P}} - \mathsf{B}_0\right)$. This is illustrated in Fig. 3(b).

C. SIGNAL MODEL

The Nakagami distribution has been used to model small scale fading for indoor mmWave propagation in prior work [48], [49]. The received power gain due to fading is then a Gamma distributed random variable. We assume the power gains $\{h_i\}$ due to fading for the wireless links from $\{\mathsf{T}_i\}$ to the reference receiver are independent and identically distributed normalized Gamma random variable with parameter m. The reference signal link of (fixed) length $d_0 = \sqrt{r_0^2 + z_0^2}$ is assumed to be unblocked by the reference user's body. Given the reference user's on-body signal link length is small (typically less than one meter) this assumption is reasonable. We would like to point out here that,

in practice, the signal link can still be occluded by the reference user's physical activity like hand movements, gait, posture etc. In the absence of a more elaborate but tractable stochastic model to incorporate these aspects based on measurement data, we assume the on-body reference signal link is unblocked. For the assumed human body model in Fig. 4 and given d, ψ_0, r_0 and W, the reference signal is unblocked whenever

$$r_0 \leq 2\sqrt{d^2 - \left(\frac{W}{2}\right)^2}. \tag{3}$$

Additionally, letting $r_0 = \sqrt{d^2 - \left(\frac{W}{2}\right)^2}$, we have

$$\phi_0^{\mathsf{a}} = \psi_0 - \frac{\pi}{2} - \arcsin\left(\frac{r_0}{2d}\right). \tag{4}$$

The condition in (3) and the derivation of (4) can be understood using the illustration of reference signal link's geometry in Fig. 4.

The path-loss exponent of the signal link is denoted α_{L}, where the subscript L denotes line-of-sight (LOS). This is in line with our assumption that the on-body reference signal link is unblocked. The non-LOS (NLOS) path-loss exponent is denoted as α_{N}, the relevance of which is explained momentarily. Such a differentiation in the path-loss exponents has been supported by indoor measurement campaigns [31]. The fade gain h_0 of the reference link is also assumed to be a normalized Gamma distributed random variable with parameter m. The path-loss function for the link from T_i to the reference receiver depends on the relative position of T_i with respect to R_0 and is denoted as $\ell(\mathsf{R}_0, \mathsf{T}_i)$. All transmitters are assumed to be transmitting at a constant transmit power. For example, this could be the maximum transmit power of devices as set out by regulations, in which case this would be a worst case scenario. The noise power normalized by the signal power observed at a reference distance is denoted as σ^2.

The transmitters and receivers are assumed to have directional antennas. The antenna array pattern is characterized by four parameters - the azimuth beam-width θ^{a}, the beam-width of the antenna main-lobe in the elevation θ^{e}, the main-lobe gain G within the beam-width, and the side-lobe gain g outside the main-lobe as shown in Fig. 5. We use subscripts t and r to denote the antenna parameters at the transmitter and the receiver, respectively. The transmitter main-lobe of T_i is assumed to be pointed in the direction given by the azimuth angle ϕ_i^{a} and elevation ϕ_i^{e}. In this model, omni-directional transmission and reception is a special case with $G = g = 1$.

The receiver-transmitter pair associated with user i are assumed to be aligned. From the reference receiver's perspective, this assumption leads to a random transmit gain for the interference from T_i as seen at R_0. Defining $p_{\mathsf{M}} = \frac{\theta_{\mathsf{t}}^{\mathsf{a}}}{2\pi}\sin\left(\frac{\theta_{\mathsf{t}}^{\mathsf{e}}}{2}\right)$, the transmit antenna gain from the i^{th} interferer can be represented using a discrete random variable $G_{\mathsf{t},i}$ as follows

$$G_{\mathsf{t},i} = \begin{cases} G_{\mathsf{t}} & \text{w.p. } p_{\mathsf{M}} \\ g_{\mathsf{t}} & \text{w.p. } 1 - p_{\mathsf{M}}. \end{cases} \tag{5}$$

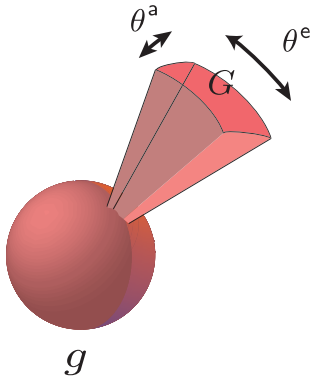

FIGURE 5. Sectorized 3D antenna gain pattern assumed for the transmitters and receivers in the wearable network.

The reference receiver's antenna main-lobe is pointed towards (fixed) azimuth angle ϕ_0^{a} and elevation angle ϕ_0^{e}, the location where the reference transmitter is positioned. Since the beam-width of the receiver antenna is $\theta_{\mathsf{r}}^{\mathsf{a}}$ and $\theta_{\mathsf{r}}^{\mathsf{e}}$ in the azimuth and elevation, respectively, the signals from all the interferers that are within an elevation angle $\phi_0^{\mathsf{e}} \pm \frac{\theta_{\mathsf{r}}^{\mathsf{e}}}{2}$ and azimuth angle $\phi_0^{\mathsf{a}} \pm \frac{\theta_{\mathsf{r}}^{\mathsf{a}}}{2}$ relative to the reference receiver R_0 are amplified by G_{r}, the main-lobe gain of R_0. Specifically, interference from the i^{th} user's transmitter T_i is amplified by a factor $G_{\mathsf{r},i}$ at the reference receiver, where

$$G_{\mathsf{r},i} = \begin{cases} G_{\mathsf{r}} & \text{if } |\measuredangle\left(\mathsf{T}_i - \mathsf{R}_0^{\mathcal{P}}\right) - \phi_0^{\mathsf{a}}| \leq \frac{\theta_{\mathsf{r}}^{\mathsf{a}}}{2} \text{ and} \\ & \quad |\arctan\left(\frac{z_0}{|\mathsf{T}_i - \mathsf{R}_0^{\mathcal{P}}|}\right) - \phi_0^{\mathsf{e}}| \leq \frac{\theta_{\mathsf{r}}^{\mathsf{e}}}{2} \\ g_{\mathsf{r}} & \text{else.} \end{cases} \tag{6}$$

D. MODELING INTERFERENCE AND BLOCKAGES

The signal from an interferer T_i to R_0 can be potentially blocked by user i, the reference user and/or user j, $j \neq i$. The blockage by user i and the reference (termed self-blockage in [39]) can occur irrespective of the locations of T_i and R_0. Specifically, self-blockage depends on whether user i and the reference user are facing each other or not. The blockage by user $j \neq i$, depends on the relative separation between T_i and $\mathsf{R}_0^{\mathcal{P}}$, and their individual positions with respect to the reflecting walls of the enclosure. For this reason, self-blockage and blockage by user $j \neq i$ are treated separately.

1) BLOCKAGE OF T_i's SIGNAL BY USER $j \neq i$

To see if user j, $j \neq i$ blocks T_i, we use the approach in [32] and define a region $\mathcal{BC}(\mathsf{B}_j) \in \mathcal{P}$ for each user relative to $\mathsf{R}_0^{\mathcal{P}}$ in $\mathcal{P}$. This region falls behind user j's body B_j as seen from

the reference receiver. Mathematically,

$$\mathcal{BC}(\mathsf{B}_j) = \left\{ z \in \mathcal{P} : |z - \mathsf{R}_0^{\mathcal{P}}|^2 \geq |\mathsf{B}_j - \mathsf{R}_0^{\mathcal{P}}|^2 - \left(\frac{W}{2}\right)^2, \right.$$
$$\left. |\measuredangle(z - \mathsf{R}_0^{\mathcal{P}}) - \measuredangle(\mathsf{B}_j - \mathsf{R}_0^{\mathcal{P}})| \leq \arcsin\left(\frac{W}{2|\mathsf{B}_j - \mathsf{R}_0^{\mathcal{P}}|}\right) \right\}, \quad (7)$$

and we refer this region as the *blocking cone* of B_j. The concept of blocking cone is illustrated in Fig. 6. Note that, using (7), we can also define the blocking cone of the reference user which is denoted as $\mathcal{BC}(\mathsf{B}_0)$. We denote T_i as *strong* if its direct and wall reflected paths do not fall in the blocking cone $\mathcal{BC}(\mathsf{B}_j)$, $j \neq i$. Otherwise, T_i is denoted as a *weak* interferer. Since B_j is uniformly distributed in $\mathcal{P}$, the interfering transmitters located farther away from $\mathsf{R}_0^{\mathcal{P}}$ have a higher chance of being a weak interferer. For analytic tractability, we define a threshold distance $r_{\mathsf{B}}(\mathsf{R}_0^{\mathcal{P}})$ around $\mathsf{R}_0^{\mathcal{P}}$ in $\mathcal{P}$ such that if $|\mathsf{R}_0^{\mathcal{P}} - \mathsf{T}_i| \leq r_{\mathsf{B}}(\mathsf{R}_0^{\mathcal{P}})$, T_i is a strong interferer. Having $|\mathsf{R}_0^{\mathcal{P}} - \mathsf{T}_i| > r_{\mathsf{B}}(\mathsf{R}_0^{\mathcal{P}})$ implies that there always exists some user $j \neq i$ that blocks the direct and wall-reflected propagation paths from T_i to R_0. An illustration describing this modeling assumption is shown in Fig. 7. This threshold-distance-based model captures the blockage effects due to a third user j for the interference signal from user i as experienced at the reference receiver.

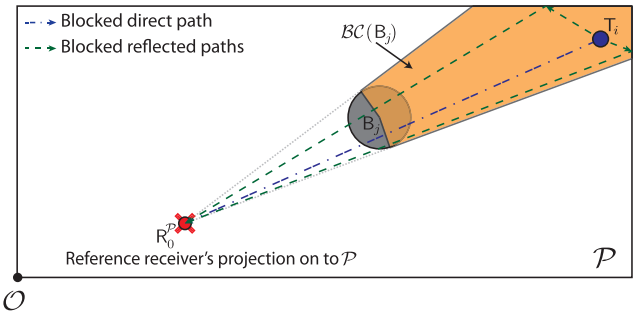

FIGURE 6. Illustration of a blocking cone showing the direct and wall-reflected paths of T_i getting blocked by B_j.

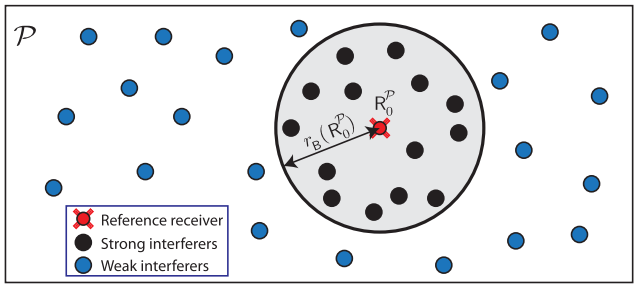

FIGURE 7. Illustration showing the threshold distance $r_{\mathsf{B}}(\mathsf{R}_0^{\mathcal{P}})$ based classification of interferers into strong and weak interferers. Interferes whose horizontal separation from the reference receiver is smaller than $r_{\mathsf{B}}(\mathsf{R}_0^{\mathcal{P}})$ are strong.

By definition, T_i is a strong interferer whenever $|\mathsf{R}_0^{\mathcal{P}} - \mathsf{T}_i| \leq r_{\mathsf{B}}(\mathsf{R}_0^{\mathcal{P}})$, and there exists no $\mathsf{B}_j, j \neq i$ in the path

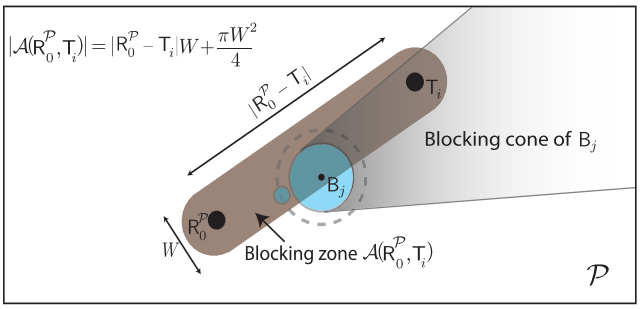

(a)

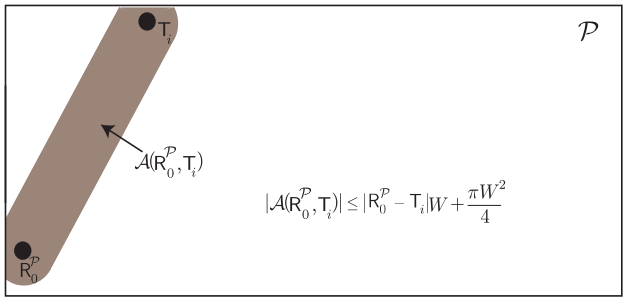

(b)

FIGURE 8. Figures showing the blocking zone $\mathcal{A}(\mathsf{R}_0^{\mathcal{P}}, \mathsf{T}_i)$ when the devices are away from the reflecting walls, and otherwise. A potential blockage B_j within $\mathcal{A}(\mathsf{R}_0^{\mathcal{P}}, \mathsf{T}_i)$ and its blocking cone are also shown for illustration. (a) Case when T_i and $\mathsf{R}_0^{\mathcal{P}}$ are away from the reflecting walls. The wall-reflected paths have lengths far larger than the direct path length and hence are not considered. (b) Case when T_i and $\mathsf{R}_0^{\mathcal{P}}$ are near the reflecting walls. The area of the region $\mathcal{A}(\mathsf{R}_0^{\mathcal{P}}, \mathsf{T}_i)$ is not fully defined by the horizontal separation between $\mathsf{R}_0^{\mathcal{P}}$ and T_i now.

from T_i to $\mathsf{R}_0^{\mathcal{P}}$. To evaluate $r_{\mathsf{B}}(\mathsf{R}_0^{\mathcal{P}})$, we use the illustration in Fig. 8(a), which shows T_i getting blocked by a user $j \neq i$ whenever user j (center of B_j) is located anywhere in the region $\mathcal{A}(\mathsf{R}_0^{\mathcal{P}}, \mathsf{T}_i)$ [34]. Since the users are assumed to be drawn from Φ, the probability that there is no user in the region $\mathcal{A}(\mathsf{R}_0^{\mathcal{P}}, \mathsf{T}_i)$ is $\exp(-\lambda|\mathcal{A}(\mathsf{R}_0^{\mathcal{P}}, \mathsf{T}_i)|)$, where $|\mathcal{A}(\mathsf{R}_0^{\mathcal{P}}, \mathsf{T}_i)|$ is the area of $\mathcal{A}(\mathsf{R}_0^{\mathcal{P}}, \mathsf{T}_i)$. The shape of $\mathcal{A}(\mathsf{R}_0^{\mathcal{P}}, \mathsf{T}_i)$ varies with $\mathsf{R}_0^{\mathcal{P}}$ (and T_i). In particular, the variation in the shape and hence the area $|\mathcal{A}(\mathsf{R}_0^{\mathcal{P}}, \mathsf{T}_i)|$ is more pronounced when one or both of $\mathsf{R}_0^{\mathcal{P}}$ and T_i are near the walls as shown in Fig. 8(b). Hence, the quantity $|\mathcal{A}(\mathsf{R}_0^{\mathcal{P}}, \mathsf{T}_i)|$ required to evaluate the probability that the interferer T_i is blocked from the reference receiver is not fully defined by the distance between $\mathsf{R}_0^{\mathcal{P}}$ and T_i. This implies the distance-dependent blockage model used in prior work to characterize mmWave outdoor network may not directly apply to indoor communication using mmWave. For indoor mmWave communication, however, the effect of wall-reflections - which results in a near LOS signal propagation - is higher when the receiver and/or the interfering transmitter are closer to the wall (Fig. 9(a)). In a densely crowded environment, since the reflected interference signals need to propagate through a longer path, the probability that the onward and reflected paths for the interference bouncing off a wall are not blocked is higher. This results in a larger area $\mathcal{A}'(\mathsf{R}_0^{\mathcal{P}}, \mathsf{T}_i)$ as illustrated in Fig. 9(b).

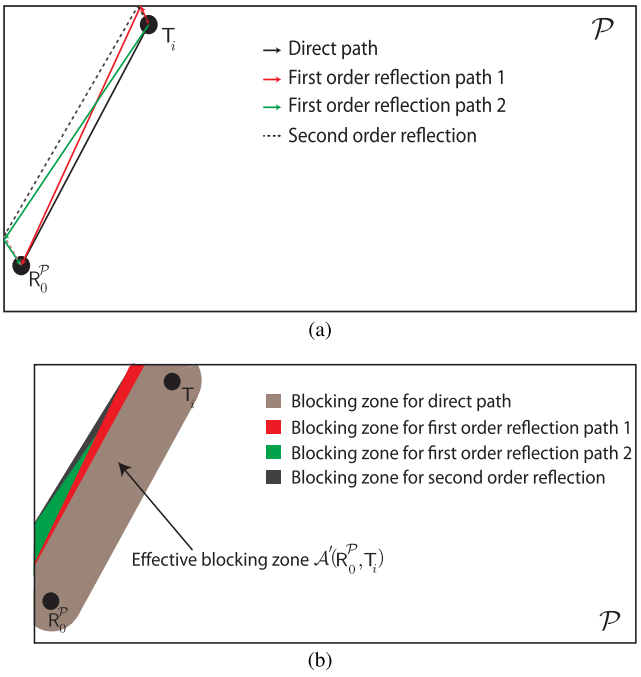

FIGURE 9. Figures showing the effective blocking zone $\mathcal{A}'(\mathsf{R}_0^{\mathcal{P}}, \mathsf{T}_i)$ when T_i and $\mathsf{R}_0^{\mathcal{P}}$ are near from the walls. (a) The predominant 1^{st} and 2^{nd} order reflections when T_i and $\mathsf{R}_0^{\mathcal{P}}$ are near the walls. Only those reflected paths whose path lengths are close to the direct path length are shown. (b) The actual blocking zone $\mathcal{A}'(\mathsf{R}_0^{\mathcal{P}}, \mathsf{T}_i)$ when T_i and $\mathsf{R}_0^{\mathcal{P}}$ are near the reflecting walls.

Assumption 1: The actual area of $\mathcal{A}'(\mathsf{R}_0^{\mathcal{P}}, \mathsf{T}_i)$ can be approximated by the area seen by receiver-transmitter pair positioned away from the reflecting walls so that

$$|\mathcal{A}'(\mathsf{R}_0^{\mathcal{P}}, \mathsf{T}_i)| \approx |\mathsf{R}_0^{\mathcal{P}} - \mathsf{T}_i| W + \frac{\pi W^2}{4}. \tag{8}$$

With this assumption, the blockage probability $p_{\mathsf{b}}\left(\mathsf{R}_0^{\mathcal{P}}, \mathsf{T}_i\right)$ of a user i due to user $j \neq i$ is a function of only the separation between $\mathsf{R}_0^{\mathcal{P}}$ and T_i. This is evaluated as

$$p_{\mathsf{b}}\left(\mathsf{R}_0^{\mathcal{P}}, \mathsf{T}_i\right) = 1 - \exp\left(-\lambda\left(|\mathsf{R}_0^{\mathcal{P}} - \mathsf{T}_i| W + \frac{\pi W^2}{4}\right)\right). \tag{9}$$

We next evaluate the threshold distance $r_{\mathsf{B}}(\mathsf{R}_0^{\mathcal{P}})$. This is computed in such a way that the average number of interferers whose direct and reflected paths are not blocked are preserved. The average number of strong interferers $\rho(\mathsf{R}_0)$ as seen from R_0 is such that

$$\begin{aligned}\frac{\rho(\mathsf{R}_0)}{\lambda} &= \int_{z\in\mathcal{P}} \left(1 - p_{\mathsf{b}}(\mathsf{R}_0^{\mathcal{P}}, z)\right) \mathrm{d}z \\ &= \int_{x=0}^{L}\int_{y=0}^{B} \exp\left(-\lambda\left(|\mathsf{R}_0^{\mathcal{P}} - (x+\mathrm{j}y)| W + \frac{\pi W^2}{4}\right)\right) \mathrm{d}y\mathrm{d}x.\end{aligned} \tag{10}$$

The mean number of interferers in a disk of radius $r_{\mathsf{B}}(\mathsf{R}_0^{\mathcal{P}})$ around $\mathsf{R}_0^{\mathcal{P}}$ is $\lambda\pi r_{\mathsf{B}}^2(\mathsf{R}_0^{\mathcal{P}})$, so that equating the mean number of strong interferers leads to

$$r_{\mathsf{B}}(\mathsf{R}_0^{\mathcal{P}}) = \left[\frac{\rho(\mathsf{R}_0)}{\pi\lambda}\right]^{\frac{1}{2}}. \tag{11}$$

We denote this disk around $\mathsf{R}_0^{\mathcal{P}}$ as $\mathcal{B}\left(\mathsf{R}_0^{\mathcal{P}}, r_{\mathsf{B}}(\mathsf{R}_0^{\mathcal{P}})\right)$. When $\mathsf{R}_0^{\mathcal{P}}$ is near the boundary of $\mathcal{P}$, parts of $\mathcal{B}\left(\mathsf{R}_0^{\mathcal{P}}, r_{\mathsf{B}}(\mathsf{R}_0^{\mathcal{P}})\right)$ lie outside $\mathcal{P}$. In such a scenario, given that the impact of reflections from the walls is significant, we continue to assume that $\mathcal{B}\left(\mathsf{R}_0^{\mathcal{P}}, r_{\mathsf{B}}(\mathsf{R}_0^{\mathcal{P}})\right)$ is a complete disk and allow T_i to lie outside $\mathcal{P}$. This is tantamount to modeling the wall reflections as signals emanating from shadow transmitters located at the reflection image locations corresponding to the actual strong interferers in $\mathcal{P}$. Note that when $\mathsf{R}_0^{\mathcal{P}}$ is close to a corner, there can be first and second order reflection sources within $\mathcal{B}\left(\mathsf{R}_0^{\mathcal{P}}, r_{\mathsf{B}}(\mathsf{R}_0^{\mathcal{P}})\right)$. For ease of analysis, we further assume that (reflection images and actual) strong interferers are independently and uniformly distributed within $\mathcal{B}\left(\mathsf{R}_0^{\mathcal{P}}, r_{\mathsf{B}}(\mathsf{R}_0^{\mathcal{P}})\right)$. This is illustrated in Fig 10.

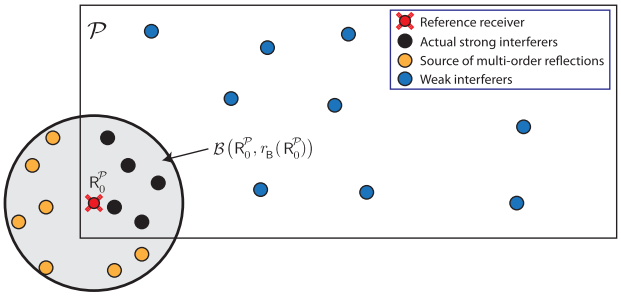

FIGURE 10. Plot showing the region $\mathcal{B}\left(\mathsf{R}_0^{\mathcal{P}}, r_{\mathsf{B}}(\mathsf{R}_0^{\mathcal{P}})\right)$, when the reference user is near a reflecting wall.

2) SELF BODY-BLOCKAGE

Self-blockage of the $\mathsf{T}_i - \mathsf{R}_0$ link occurs if $\mathsf{T}_i \in \mathcal{BC}(\mathsf{B}_i)$ and/or $\mathsf{T}_i \in \mathcal{BC}(\mathsf{B}_0)$. This results in a constant attenuation of B_{L} (linear scale), for each number of self-blockages. Such a model has been used in [39] in the context of mmWave cellular systems. In [39], self-blockage accounts for roughly 40 dB loss in SINR. Unlike the cellular case where the number of self-blockages in a link can be 0 or 1, in the mmWave wearables context, the number of self-blockages in a link can be either 0, 1 or 2. Self-blockage is the only source of blockage for strong interferers in our model. For a weak interferer, self-blockage further degrades the signal strength in addition to blockages due to other users. Hence, we assume the propagation is NLOS with a path-loss exponent $\alpha_{\mathsf{N}} > \alpha_{\mathsf{L}}$. If a weak interferer is not self-blocked, we assume the propagation path via ceiling reflection prevents the channel from being NLOS.

We summarize our blockage-based path-loss model for a general $\mathsf{T}_i \in \mathcal{P}$ next. The path length of the ceiling reflected signal from T_i to R_0 is denoted by

$$\|\mathsf{R}_0 - \mathsf{T}_i\|_c = \sqrt{|\mathsf{R}_0^{\mathcal{P}} - \mathsf{T}_i|^2 + (2d_{\mathsf{h}} - z_0)^2}, \tag{12}$$

and the Euclidean distance between T_i and R_0 is denoted by

$$\|\mathsf{R}_0 - \mathsf{T}_i\| = \sqrt{|\mathsf{R}_0^{\mathcal{P}} - \mathsf{T}_i|^2 + z_0^2}. \tag{13}$$

Denoting the number of self-blockages in the $\mathsf{T}_i - \mathsf{R}_0$ link by s and using $\mathbf{1}_A$ to denote the indicator function of event A, the path-loss function $\ell(\mathsf{R}_0, \mathsf{T}_i)$ can be classified into any one of the following:

Case A: When T_i is a strong interferer,

$$\ell(\mathsf{R}_0, \mathsf{T}_i) = \|\mathsf{R}_0 - \mathsf{T}_i\|^{-\alpha_{\mathsf{L}}} \mathsf{B}_{\mathsf{L}}^{-s}. \tag{14}$$

Case B: When T_i is a weak interferer

$$\ell(\mathsf{R}_0, \mathsf{T}_i) = \|\mathsf{R}_0 - \mathsf{T}_i\|_c^{-\alpha_{\mathsf{L}}} \mathbf{1}_{\{s=0\}} + \|\mathsf{R}_0 - \mathsf{T}_i\|^{-\alpha_{\mathsf{N}}} \mathbf{1}_{\{s\neq 0\}}. \tag{15}$$

Note that we do not consider the reflection from ceiling in Case A. This is in line with our assumption that when T_i is a strong interferer located within close proximity to $\mathsf{R}_0^{\mathcal{P}}$ in $\mathcal{P}$, the signal bouncing off the ceiling is less significant compared to the direct and wall-reflected signals. The effect of reflections from the ceiling is assumed to be substantial only when the users are facing each other and when $|\mathsf{R}_0^{\mathcal{P}} - \mathsf{T}_i| > r_{\mathsf{B}}(\mathsf{R}_0^{\mathcal{P}})$. The NLOS propagation in Case B-2 coarsely also accounts for all possible scattering and diffraction that dominates when an interferer is weak and self-blocked. This is the intuition behind the different cases for the path-loss function.

To conclude the discussion on interference and blockage modeling, we note that now we have a region $\mathcal{B}\left(\mathsf{R}_0^{\mathcal{P}}, r_{\mathsf{B}}(\mathsf{R}_0^{\mathcal{P}})\right)$ around $\mathsf{R}_0^{\mathcal{P}}$ such that the interference signal (direct or wall-reflected) from T_i located within $\mathcal{B}\left(\mathsf{R}_0^{\mathcal{P}}, r_{\mathsf{B}}(\mathsf{R}_0^{\mathcal{P}})\right)$ is never blocked by B_j, $j \neq i$. Further, the direct and wall-reflected paths for the interference from T_i outside $\mathcal{B}\left(\mathsf{R}_0^{\mathcal{P}}, r_{\mathsf{B}}(\mathsf{R}_0^{\mathcal{P}})\right)$ is always blocked by some user $j \neq i$.

IV. SINR COVERAGE PROBABILITY

In this section, the reliability of the mmWave link of the reference user is characterized by evaluating the SINR distribution of the reference link as a function of the reference user's location within the enclosure. The SINR coverage probability for an SINR threshold γ is defined as the probability that the receiver SINR is greater than γ. The SINR seen at the reference receiver R_0 when its body is facing in the direction ψ_0 is

$$\Gamma(\mathsf{R}_0, \psi_0) = \frac{h_0 G_{\mathsf{t}} G_{\mathsf{r}} d_0^{-\alpha_{\mathsf{L}}}}{\sigma^2 + \sum_{i\in\Phi} G_{\mathsf{t},i} G_{\mathsf{r},i} h_i \ell(\mathsf{R}_0, \mathsf{T}_i)}. \tag{16}$$

Note that in (16), the term $\ell(\mathsf{R}_0, \mathsf{T}_i)$ captures the effect of the reference user's body orientation ψ_0 as defined in (14)-(15). Denoting $\tilde{\gamma} = \frac{d_0^{\alpha_{\mathsf{L}}}}{G_{\mathsf{t}} G_{\mathsf{r}}}$, the complementary cumulative distribution function (CCDF) of SINR, which is also referred to as the SINR coverage probability [40], is

$$\begin{aligned}
&\mathbb{P}\left(\Gamma(\mathsf{R}_0, \psi_0) > \gamma\right) \\
&= \mathbb{P}\left(h_0 > \tilde{\gamma}\left(\sigma^2 + \sum_{i\in\Phi} G_{\mathsf{t},i} G_{\mathsf{r},i} h_i \ell(\mathsf{R}_0 - \mathsf{T}_i)\right)\right) \\
&\leq 1 - \mathbb{E}_\Phi\left[\left(1 - e^{-m\tilde{m}\tilde{\gamma}\left(\sigma^2 + \sum_{i\in\Phi} G_{\mathsf{t},i} G_{\mathsf{r},i} h_i \ell(\mathsf{R}_0, \mathsf{T}_i)\right)}\right)^m\right].
\end{aligned} \tag{17}$$

In (17), we have used a tight lower bound for the CDF of the normalized gamma random variable [50], with $\tilde{m} = (m!)^{\frac{-1}{m}}$. Denoting

$$I_\Phi^{\mathsf{SI}} = \sum_{i\in\mathcal{B}\left(\mathsf{R}_0^{\mathcal{P}}, r_{\mathsf{B}}(\mathsf{R}_0^{\mathcal{P}})\right)} G_{\mathsf{t},i} G_{\mathsf{r},i} h_i \ell(\mathsf{R}_0, \mathsf{T}_i) \text{ and} \tag{18}$$

$$I_\Phi^{\mathsf{WI}} = \sum_{i\in\Phi\setminus\mathcal{B}\left(\mathsf{R}_0^{\mathcal{P}}, r_{\mathsf{B}}(\mathsf{R}_0^{\mathcal{P}})\right)} G_{\mathsf{t},i} G_{\mathsf{r},i} h_i \ell(\mathsf{R}_0, \mathsf{T}_i), \tag{19}$$

and using the binomial expansion followed by splitting the strong and weak interference terms, we can write (17) as

$$\begin{aligned}
\mathbb{P}\left(\Gamma(\mathsf{R}_0, \psi_0) > \gamma\right) = \sum_{k=1}^{m} \binom{m}{k} (-1)^{k+1} e^{-km\tilde{m}\tilde{\gamma}\sigma^2} \\
\times \mathbb{E}_\Phi\left[e^{-km\tilde{m}\tilde{\gamma} I_\Phi^{\mathsf{SI}}}\right] \mathbb{E}_\Phi\left[e^{-km\tilde{m}\tilde{\gamma} I_\Phi^{\mathsf{WI}}}\right].
\end{aligned} \tag{20}$$

The expectation terms in (20) are as given in Theorem 1 and Theorem 2, which make use of the following lemmas.

Lemma 1: The probability p_s that $\mathsf{T}_i \in \mathcal{B}\left(\mathsf{R}_0^{\mathcal{P}}, r_{\mathsf{B}}(\mathsf{R}_0^{\mathcal{P}})\right)$ experiences s human body (self) blockages is given by

$$p_s = \begin{cases} (1 - p_{\mathsf{b}}^{\text{self}})^2 & s = 0 \\ 2p_{\mathsf{b}}^{\text{self}}(1 - p_{\mathsf{b}}^{\text{self}}) & s = 1 \\ \left(p_{\mathsf{b}}^{\text{self}}\right)^2 & s = 2 \end{cases}, \tag{21}$$

where $p_{\mathsf{b}}^{\text{self}} = \frac{1}{\pi} \arcsin\left(\frac{W}{2d}\right)$, and the probability $q(\mathsf{R}_0, \psi_0)$ that both T_i and R_0 are facing each other when $\mathsf{T}_i \in \mathcal{P} \setminus \mathcal{B}\left(\mathsf{R}_0^{\mathcal{P}}, r_{\mathsf{B}}(\mathsf{R}_0^{\mathcal{P}})\right)$ is given by

$$q(\mathsf{R}_0, \psi_0) = \left(1 - p_{\mathsf{b}}^{\text{self}}\right)\left(1 - q_1(\mathsf{R}_0, \psi_0)\right), \tag{22}$$

where

$$q_1(\mathsf{R}_0, \psi_0) = \frac{|\mathcal{BC}(\mathsf{B}_0) \setminus \mathcal{B}\left(\mathsf{R}_0^{\mathcal{P}}, r_{\mathsf{B}}(\mathsf{R}_0^{\mathcal{P}})\right)|}{LB - |\mathcal{P} \cap \mathcal{B}\left(\mathsf{R}_0^{\mathcal{P}}, r_{\mathsf{B}}(\mathsf{R}_0^{\mathcal{P}})\right)|}. \tag{23}$$

Proof: See Appendix A. ∎

The term $q_1(\mathsf{R}_0, \psi_0)$ in (23) denotes the probability that a weak interferer is in the blocking cone of B_0 given that it lies outside $\mathcal{B}\left(\mathsf{R}_0^{\mathcal{P}}, r_{\mathsf{B}}(\mathsf{R}_0^{\mathcal{P}})\right)$ in $\mathcal{P}$. This probability is obtained as the ratio of the two areas given in the numerator and denominator in (23). Note that, for a given $\mathcal{B}\left(\mathsf{R}_0^{\mathcal{P}}, r_{\mathsf{B}}(\mathsf{R}_0^{\mathcal{P}})\right)$ (computed using (11)), these areas (23) need to be evaluated via numerical integration.

We use the following notation ((24) - (27)) in Lemma 2:

$$r_{\max} = z_0 \cot\left(\phi_0^{\mathsf{e}} - \frac{\theta_{\mathsf{r}}^{\mathsf{e}}}{2}\right), \tag{24}$$

$$r_{\min} = z_0 \cot\left(\phi_0^{\mathsf{e}} + \frac{\theta_{\mathsf{r}}^{\mathsf{e}}}{2}\right). \quad (25)$$

Quantities in (24) and (25) together define a region in $\mathcal{P}$ which falls within the elevation beam-width of reference receiver's antenna.

$$\hat{\mathcal{P}} = \mathcal{P} \setminus \mathcal{B}\left(\mathsf{R}_0^{\mathcal{P}}, r_{\mathsf{B}}(\mathsf{R}_0^{\mathcal{P}})\right) \text{ and} \quad (26)$$

$$\Upsilon(\phi_0^{\mathsf{a}}) = \left\{ z \in \hat{\mathcal{P}} : \measuredangle z \in \left[\phi_0^{\mathsf{a}} - \frac{\theta_{\mathsf{r}}^{\mathsf{a}}}{2}, \phi_0^{\mathsf{a}} + \frac{\theta_{\mathsf{r}}^{\mathsf{a}}}{2}\right] \right\}. \quad (27)$$

The set in (27) denotes a region outside $\mathcal{B}\left(\mathsf{R}_0^{\mathcal{P}}, r_{\mathsf{B}}(\mathsf{R}_0^{\mathcal{P}})\right)$ in $\mathcal{P}$ that falls in the main-lobe of the reference receiver in the azimuth.

Lemma 2: The probability $p_{\mathrm{rx}}^{\mathsf{SI}}$ that a strong interferer is within the main-lobe of the reference receiver is

$$p_{\mathrm{rx}}^{\mathsf{SI}} = \frac{\theta_{\mathsf{r}}^{\mathsf{a}}}{2\pi}\left(\frac{\min\left(r_{\mathsf{B}}(\mathsf{R}_0^{\mathcal{P}}), r_{\max}\right)^2 - r_{\min}^2}{r_{\mathsf{B}}^2(\mathsf{R}_0^{\mathcal{P}})}\right). \quad (28)$$

The probability $p_{\mathrm{rx}}^{\mathsf{WI}}$ that a weak interferer is within the main-lobe of the reference receiver is

$$p_{\mathrm{rx}}^{\mathsf{WI}} = \frac{|\Upsilon(\phi_0^{\mathsf{a}})|}{|\hat{\mathcal{P}}|}\left(1 - \frac{|\mathcal{P} \setminus \mathcal{B}\left(\mathsf{R}_0^{\mathcal{P}}, \max(r_{\mathsf{B}}(\mathsf{R}_0^{\mathcal{P}}), r_{\mathsf{max}})\right)|}{|\mathcal{P} \setminus \mathcal{B}\left(\mathsf{R}_0^{\mathcal{P}}, r_{\mathsf{B}}(\mathsf{R}_0^{\mathcal{P}})\right)|}\right). \quad (29)$$

Proof: See Appendix B. ∎

In (29), areas of regions have to be evaluated numerically. We define the following vector arrays for ease of notation in Theorem 1 and Theorem 2:

$$\mu = \begin{bmatrix} p_{\mathsf{M}} p_{\mathrm{rx}}^{\mathsf{SI}} \\ (1-p_{\mathsf{M}})\, p_{\mathrm{rx}}^{\mathsf{SI}} \\ p_{\mathsf{M}}\left(1 - p_{\mathrm{rx}}^{\mathsf{SI}}\right) \\ (1-p_{\mathsf{M}})\left(1 - p_{\mathrm{rx}}^{\mathsf{SI}}\right) \end{bmatrix}, \quad \nu = \begin{bmatrix} p_{\mathsf{M}} p_{\mathrm{rx}}^{\mathsf{WI}} \\ (1-p_{\mathsf{M}})\, p_{\mathrm{rx}}^{\mathsf{WI}} \\ p_{\mathsf{M}}\left(1 - p_{\mathrm{rx}}^{\mathsf{WI}}\right) \\ (1-p_{\mathsf{M}})\left(1 - p_{\mathrm{rx}}^{\mathsf{WI}}\right) \end{bmatrix}, \quad (30)$$

$$\mathcal{G} = \begin{bmatrix} G_{\mathsf{t}}G_{\mathsf{r}} & g_{\mathsf{t}}G_{\mathsf{r}} & G_{\mathsf{t}}g_{\mathsf{r}} & g_{\mathsf{t}}g_{\mathsf{r}} \end{bmatrix}. \quad (31)$$

We use subscript j to denote a vector array's j^{th} entry.

Theorem 1: Denoting $\tilde{R} = r_{\mathsf{B}}(\mathsf{R}_0^{\mathcal{P}})$ for simplicity, and

$$A_{j,s} = \frac{\tilde{R}^2}{2} - \int_0^{\tilde{R}} \left(1 + \frac{k\tilde{m}\tilde{\gamma}\mathcal{G}_j}{\left(r^2 + z_0^2\right)^{\frac{\alpha_{\mathsf{L}}}{2}} \mathsf{B}_{\mathsf{L}}^s}\right)^{-m} r\,\mathrm{d}r, \quad (32)$$

the expectation term corresponding to the strong interferers in (20) *can be expressed as follows*

$$\mathbb{E}_\Phi\left[e^{-km\tilde{m}\tilde{\gamma}I_\Phi^{\mathsf{SI}}}\right] = \exp\left[-2\pi\lambda\left(p_0\sum_{j=1}^{4}\mu_j A_{j,0} + \frac{p_1}{2}\sum_{j=1}^{4}\mu_j A_{j,1} + \frac{p_1}{2\left(1-p_{\mathrm{rx}}^{\mathsf{SI}}\right)}\sum_{j=3}^{4}\mu_j A_{j,1} + \frac{p_2}{\left(1-p_{\mathrm{rx}}^{\mathsf{SI}}\right)}\sum_{j=3}^{4}\mu_j A_{j,2}\right)\right]. \quad (33)$$

Proof: See Appendix C. ∎

Theorem 2: Defining

$$C_1 = |\hat{\mathcal{P}}| - \sum_{j=1}^{4}\nu_j \int_{z\in\hat{\mathcal{P}}} \left(1 + \frac{k\tilde{m}\tilde{\gamma}\mathcal{G}_j}{\|\mathsf{R}_0 - z\|_c^{\alpha_{\mathsf{L}}}}\right)^{-m} \mathrm{d}z, \quad (34)$$

$$\& \; C_2 = |\hat{\mathcal{P}}| - \sum_{j=3}^{4}\frac{\nu_j}{\left(1-p_{\mathrm{rx}}^{\mathsf{WI}}\right)} \int_{z\in\hat{\mathcal{P}}} \left(1 + \frac{k\tilde{m}\tilde{\gamma}\mathcal{G}_j}{\|\mathsf{R}_0 - z\|^{\alpha_{\mathsf{N}}}}\right)^{-m} \mathrm{d}z, \quad (35)$$

the expectation term corresponding to the weak interferers in (20) *simplifies to*

$$\mathbb{E}_\Phi\left[e^{-km\tilde{m}\tilde{\gamma}I_\Phi^{\mathsf{WI}}}\right] = \exp\left[-\lambda\left(q(\mathsf{R}_0,\psi_0)C_1 + (1-q(\mathsf{R}_0,\psi_0))C_2\right)\right]. \quad (36)$$

Proof: See Appendix D. ∎

To evaluate the analytic plots of the SINR distribution for a given network dimension and user density, the threshold distance $r_{\mathsf{B}}(\mathsf{R}_0^{\mathcal{P}})$ is first computed for a given R_0. Next, based on the given body orientation ψ_0 of the reference user, the self blocking probability and the probability that an interferer falls in the main-lobe of the reference receiver are computed analytically for the strong interferers (using (21) and (28), respectively). The corresponding quantities for the weak interferers are computed using geometry and numerical integration based on (23) and (29). Using these computations and plugging the results from Theorem 1 and Theorem 2 ((33) and (36)) into (20), we compute the spatially averaged SINR coverage probability for a given receiver location R_0 and orientation angle ψ_0. Note that the results implicitly incorporate the direction in 3D where the receiver antenna is pointed, i.e., $(\phi_0^{\mathsf{a}}, \phi_0^{\mathsf{e}})$, though we do not explicitly denote that in (20). The spectral efficiency $\mathcal{C}(\mathsf{R}_0, \psi_0)$ for a given SINR can be computed as $\log_2(1 + \Gamma(\mathsf{R}_0, \psi_0))$. With the knowledge of the CCDF of SINR, the ergodic spectral efficiency $\mathbb{E}\left[\mathcal{C}(\mathsf{R}_0, \psi_0)\right]$ of the reference user's communication link can be evaluated as a function of the reference receiver location and orientation of its body.

V. SYSTEM VALIDATION AND PLOTS

In this section, simulation and numerical results that shed insights into the proposed model are discussed. Simulation results to validate the analytic expressions for spatial averages are also provided in this section. The parameters used for the results are summarized in Table 1. The default value used for $r_0 = \sqrt{d^2 - \left(\frac{W}{2}\right)^2}$, so that the reference signal link is unblocked by the reference user's body. This is also shown in Table 1. The values of the reference antenna pointing angles ϕ_0^{a} and ϕ_0^{e} are computed according to (2) and (4).

A. VALIDATION OF THE ANALYTIC MODEL VIA SIMULATION

The expression derived in Section IV, is validated against simulation and is shown in Fig. 11. As discussed earlier, the impact of reflections due to the walls of the enclosure

TABLE 1. Default values of parameters used for simulation.

Parameter	Value	Description
L	15 m	Length of the enclosure
B	5 m	Breadth of the enclosure
H	2.5 m	Height of the enclosure
d_{h}	1.5 m	Transmitters' vertical distance from ceiling
W	0.45 m	Width of user body
d	0.325 m	Distance between body center and wearable
z_0	0.5 m	Height at which receiver is positioned
r_0	0.2345 m	Horizontal separation between R_0 and T_0
λ	2 m^{-2}	Crowd density
α_{L}	2	LOS path-loss exponent
α_{N}	4	NLOS path-loss exponent
m	7	Nakagami parameter of small scale fading
B_{L}	40 dB	Self-body blockage loss

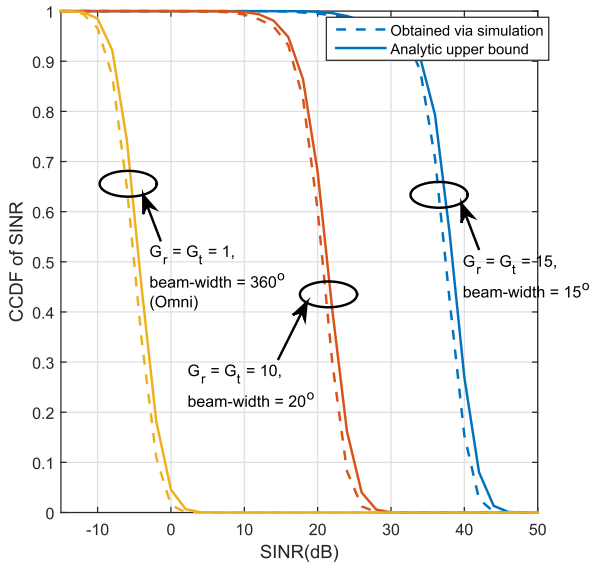

FIGURE 11. SINR distribution obtained through simulation and analytic expression when the receiver is at a corner $0.5 + \mathrm{j}0.5$ for different antenna configurations. Our proposed analytic model match well with simulation results which account for random geometry for interfering users, reflections due to the finite enclosure and small scale fading. With directional antennas, significant improvement in performance is seen.

is non-trivial for the indoor mmWave wearable network setting. Therefore, to obtain the simulation plots, phantom transmitters and user bodies were assumed to be located at the mirror image locations of the actual interferers and their corresponding human body locations, respectively using using ray optics. This effectively modeled the impact of reflection due to the walls and the ceiling of the enclosure $\mathcal{T}$ similar to [14]. To see if an interferer (actual or phantom transmitter) is blocked from the reference user's receiver, the approach elaborated in [32] was used. Note that we do not account for the actual reflection coefficient associated with the walls which is a function of the angle of incidence of the signal. Analysis in [14], however, shows that for highly reflective surfaces, the reflection coefficient is close to unity and more or less independent of the angle of incidence. Hence, merely placing phantom transmitters at the mirror image locations and assuming the same transmit power as that of the actual interferers are justified. The CCDF of the SINR is then obtained by averaging the random geometry of the user locations, small scale fading and random body orientation of the interfering users. It is seen that the analytic expression for the upper bound of SINR coverage probability is very tight and matches the simulation results very well.

Fig. 11 also shows the SINR distribution for different antenna configurations. It is seen that having larger antenna gains and highly directed transmissions and reception improve the performance significantly. This is because directional antennas reduce the probability that interferers point their main-lobes in the direction of the reference receiver's antenna main-lobe, thus reducing the effective interference, while boosting the antenna gains in the reference signal link.

B. NUMERICAL RESULTS

A plot of the mean number of strong interferers as a function of the location of the reference receiver is shown in Fig. 12. When the reference receiver is near the walls of the enclosure, the mean number of strong interferers is lower compared to that when at the center. This implies that reflections due to the walls are less significant than the direct interference caused by other users when the user density is high.

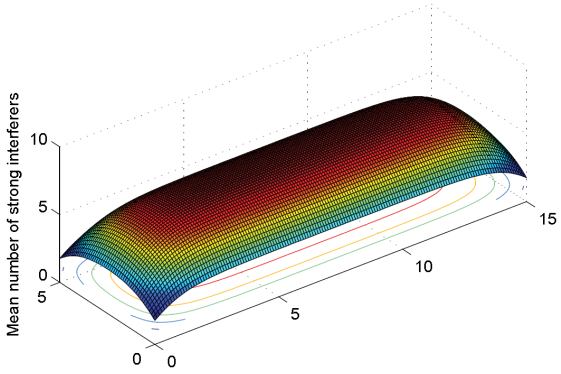

FIGURE 12. Plot showing the variation in the mean number of strong interferers seen be the reference user at various locations within the enclosure. The mean number of strong interferers is smaller when the reference user is near the walls of the enclosed region.

The dependence of system performance on the reference user body orientation is studied by plotting the average achievable rate for the cases when the reference user is at the center and near a corner (we assume $\mathsf{R}_0^{\mathcal{P}} = 0.5 + \mathrm{j}0.5$ in this case). For this, the analytic expressions derived in Section IV are used to compute the egodic spectral efficiency of the reference link. The average achievable rate is then computed by multiplying the egodic spectral efficiency with the system bandwidth which is taken to be 2.16 GHz assuming an IEEE 802.11ad like setup. The plots are shown in Fig. 13 for omni-directional antennas at the transmitters and the receivers, from which we see that the sensitivity to body orientation is more pronounced when the reference user is at corner. This means that when at a corner, turning the body to face away from

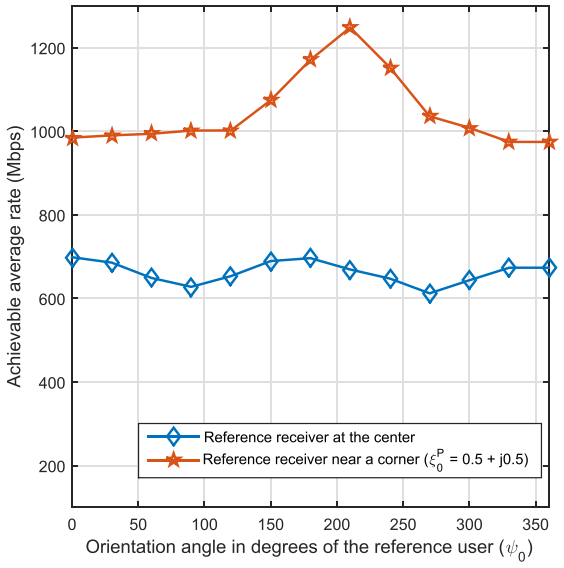

FIGURE 13. Plot showing the variation in the average achievable rate as a function of the body orientation of the reference user when located at the center and near a corner assuming omni-directional antennas are used at the devices. When the reference user is at the corner location, body orientation plays a significant role in improving achievable rate.

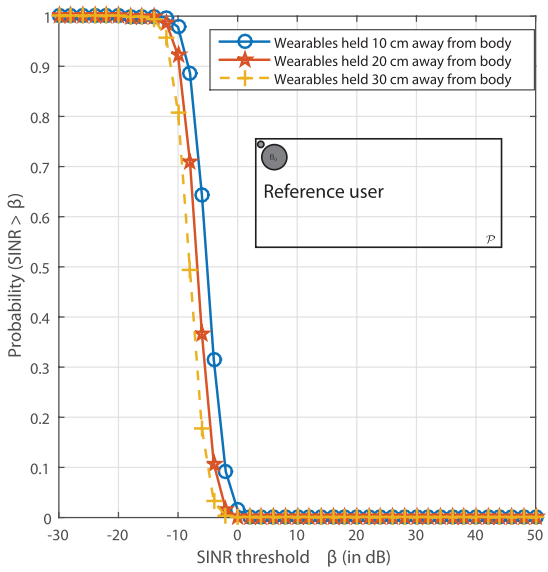

FIGURE 15. Plot showing the variation in system performance as a function of the relative separation between the user body and the wearable device. $\mathsf{R}_0^{\mathcal{P}}$, is assumed to be located at 0.5 + j4.5 (see inset picture) and the transceivers are assumed to be omni-directional. Holding the wearable devices closer to the human body improves the SINR coverage probability.

the interfering crowd ($\psi_0 = 225^o$ for $\mathsf{R}_0^{\mathcal{P}} = 0.5 + \text{j}0.5$) gives the best performance thanks to the body blockage due to the reference user's body for the mmWave interference signals.

The performance of the reference link as the reference user is positioned at various locations of the enclosure is investigated next. The location dependent SINR coverage probability is shown in Fig. 14 in the form of a heat map which is a graphical representation of data where the individual values contained in a matrix are represented as colors. In Fig. 14, an SINR threshold of -5 dB and $\psi_0 = 0^o$ are assumed for representing the SINR coverage probability as a color at reference receiver location in $\mathcal{P}$ (projection) specified by the x and y coordinates. It is seen that the best performance is obtained when the reference receiver is near the corner and facing away from the interfering crowd. This is the case when all the interferers are shielded by the reference user's body. From Fig. 14 we can also see how the interplay of reference user's body blockage and the reflections from the enclosure

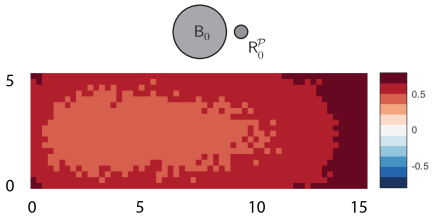

FIGURE 14. Plot showing SINR coverage probability heat map as a function of the reference location position when the reference user is facing to the right, i.e. $\psi_0 = 0^o$ and with omni-directional transceivers. The body orientation of the reference user is also shown in the figure. System performance of mmWave wearable networks in dense indoor environments heavily depends on the location.

result in significant variation in the performance seen at the reference receiver as the user moves around the crowd.

The dependence of system performance with respect to d, the relative separation between the user body and the wearable device is shown in Fig. 15 for omni-directional antennas used at the devices. We let $\mathsf{R}_0^{\mathcal{P}} = 0.5 + \text{j}4.5$ which is a corner location and take $\psi_0 = 135^o$ so that the user is facing away from the interfering crowd. The plots in Fig. 15 show that for getting improved performance in a crowded environment, the device must be positioned closer to the user. This is because the self-body blockage better helps in attenuating the interference from other wearable networks when wearable devices are held close to the user body.

To understand the interplay between the horizontal and vertical separation distance of the reference link, we show a contour plot of the average achievable rate in Fig. 16 as a function of the horizontal separation r_0 and the vertical separation z_0 of the reference signal link when the reference user is at the center of the enclosure. It is seen that the combination $z_0 > 0$ and $r_0 = 0$ gives the best performance. This scenario corresponds to having the reference receiver vertically placed above the reference receiver. It can also be seen from Fig. 16 that when $r_0 > 0$, having z_0 slightly above 0 is more advantageous than having $z_0 = 0$, i.e., having both the receiver and transmitter in the same plane ($\mathcal{P}$) is not recommended for rate performance as this scenario does not utilize the receiver antenna directivity in the elevation plane. The results in Fig. 16 assume $G_{\text{r}} = G_{\text{t}} = 10$, $g_{\text{r}} = g_{\text{t}} = 0.5$ and beam-width $= 20^o$ in the azimuth and elevation. We also assume the reference receiver is located at the center and facing towards right (i.e., $\psi_0 = 0$).

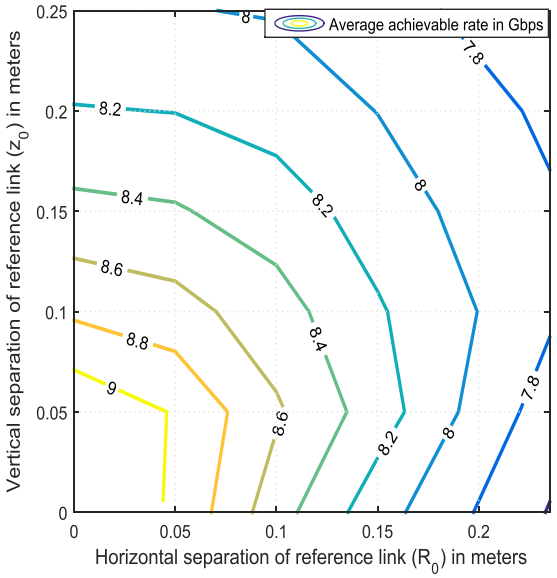

FIGURE 16. Contour plot showing the variation in average achievable rates in Gbps as a function of the horizontal and vertical separation distance between the reference receiver and reference transmitter. Vertically positioning the reference transmitter (below) and receiver (above) gives the best ergodic rate performance.

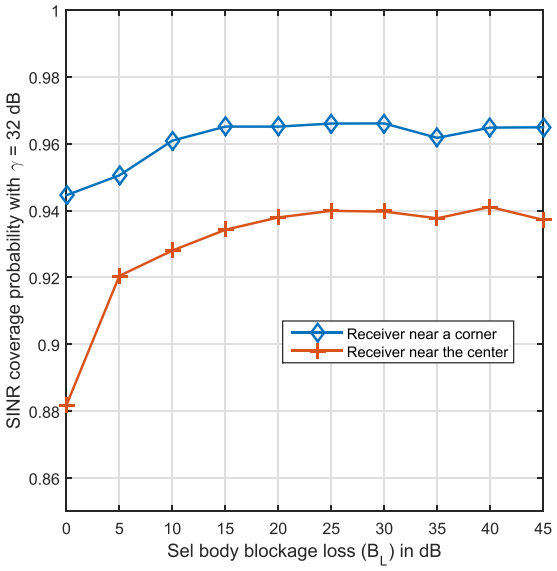

FIGURE 17. Plot showing the variation of SINR coverage probability as the self-blockage attenuation $\mathsf{B_L}$ is varied. Larger $\mathsf{B_L}$ is more helpful when the reference user is at the center.

The variation of SINR coverage probability for an SINR threshold of $\gamma = 32$ dB as the self-body blockage loss $\mathsf{B_L}$ is varied is shown in Fig. 17 when $\psi_0 = 0$. We let $G_\mathsf{r} = G_\mathsf{t} = 15$, $g_\mathsf{r} = g_\mathsf{t} = 0.1$ and beam-width $= 15^o$ in the azimuth and elevation. Two locations - one near a corner (12.5 + j0.5) and at the center are considered in Fig. 17. It is observed that while increasing $\mathsf{B_L}$ improves the coverage probability of the reference signal link, the improvement is higher when the reference receiver is at the center. This is because, since the amount of interference is more pronounced at the center, the self-blody blockage shields the reference signal better thus resulting in better SINR performance improvement compared to a corner location.

VI. CONCLUSIONS

In this paper, we developed a tractable system model to analyze the performance of mmWave-based wearable network in a densely crowded indoor environment when there is no coordination between users to control interference. We modeled the effects of human-body blockages due to other users and also the reference user. The proposed system model also captured the predominant effects of wall and ceiling reflections when the user density is high. The proposed analytic model is validated against simulations. Using the proposed path-loss model, we derived closed-form expressions for spatially averaged system performance in terms of SINR coverage and rate that can be computed as a function of location and body orientation of the reference user. We observed that the effect of body orientation is significant when the reference user is located at a corner. The peak average rate for the system was obtained when the reference user is near the corner and facing away from the interferers. We studied the impact of relative placement of the on-body receiver and transmitter and the importance of antenna directivity. We showed that when the reference receiver is placed vertically above the reference transmitter, maximum gain in performance is obtained using narrow beam directional antennas at the transmitter and receiver. Future work can consider the impact of antenna misalignment of the reference signal link as well as reference link blockage due to human user's movement.

ACKNOWLEDGEMENT

The authors thank Alexander Pyattaev and Dr. Kerstin Johnsson for their valuable suggestions and helpful discussions on the impact of human user self-blockage in the indoor mmWave wearable networks.

APPENDIX A
PROOF OF LEMMA 1

The probability that user i blocks $\mathsf{R}_0 - \mathsf{T}_i$ link is the same as the probability that $\mathsf{R}_0^{\mathcal{P}} - \mathsf{T}_i$ link is blocked by B_i in $\mathcal{P}$. Since T_i is assumed to be located uniformly at random in a radius-d circle around B_i (same as B_i being located randomly around T_i in a radius-d circle), the probability that B_i blocks T_i link is

$$p_\mathsf{b}^{\text{self}} = \frac{1}{\pi} \arcsin\left(\frac{W}{2d}\right). \tag{37}$$

An illustration explaining the derivation of $p_\mathsf{b}^{\text{self}}$ is shown in Fig. 18.

The probability that T_i falls in the blocking cone of B_0 is also $p_\mathsf{b}^{\text{self}}$ as $\mathcal{B}\left(\mathsf{R}_0^{\mathcal{P}}, r_\mathsf{B}(\mathsf{R}_0^{\mathcal{P}})\right)$ is circular with R_0 located at its center. So, the probability that both B_0 and B_i blocks T_i's interference is $p_2 = \left(p_\mathsf{b}^{\text{self}}\right)^2$, and the probability that neither user bodies block the interference is $p_0 = (1-p_\mathsf{b}^{\text{self}})^2$. Finally, p_1 can be computed to satisfy $\sum_{s=0}^{2} p_s = 1$.

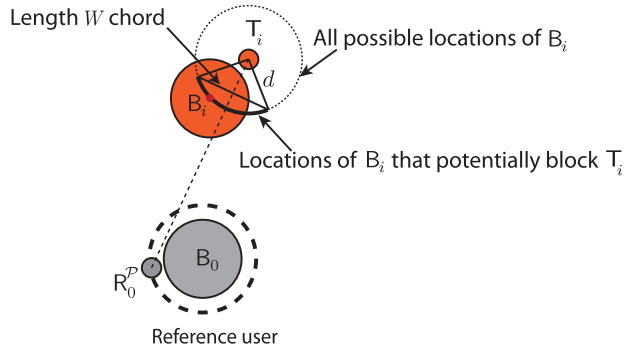

FIGURE 18. Illustration of self-blockage of $\mathsf{R}_0 - \mathsf{T}_i$ link due to B_i.

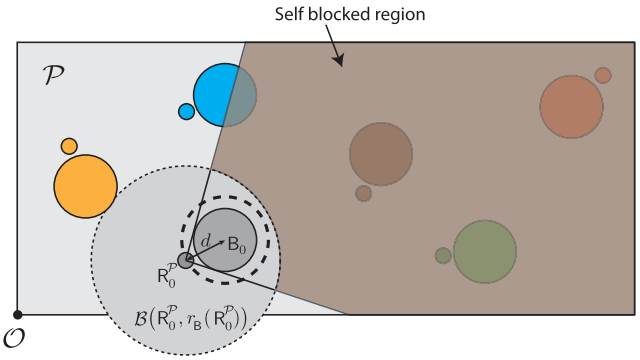

FIGURE 19. Illustration showing the (shaded) region where weak interferers are self-blocked by B_0.

To evaluate $q(\mathsf{R}_0, \psi_0)$ in the second part of the Lemma, we use the illustration shown in Fig. 19 which depicts the region in $\mathcal{P} \setminus \mathcal{B}\left(\mathsf{R}_0^{\mathcal{P}}, r_{\mathsf{B}}(\mathsf{R}_0^{\mathcal{P}})\right)$ that is blocked due to B_0. The probability that T_i is in this region (denoted as $\mathcal{BC}(\mathsf{B}_0) \setminus \mathcal{B}\left(\mathsf{R}_0^{\mathcal{P}}, r_{\mathsf{B}}(\mathsf{R}_0^{\mathcal{P}})\right)$) is $q_1(\mathsf{R}_0, \psi_0)$ given in Lemma 1. The probability that B_i blocks T_i is still $p_{\mathsf{b}}^{\text{self}}$ since it only depends on $\psi_i = \measuredangle(\psi_i - \mathsf{B}_i)$ that is uniformly random in $[0, 2\pi]$ (cf Fig. 18). So the probability that both the weak interferer T_i and z_0 are facing each other is

$$q(\mathsf{R}_0, \psi_0) = \left(1 - p_{\mathsf{b}}^{\text{self}}\right)\left(1 - q_1(\mathsf{R}_0, \psi_0)\right). \tag{38}$$

APPENDIX B
PROOF OF LEMMA 2

The interferers T_i such that $\measuredangle\mathsf{T}_i \in \left[\phi_0^{\mathsf{a}} - \frac{\theta_{\mathsf{r}}^{\mathsf{a}}}{2}, \phi_0^{\mathsf{a}} + \frac{\theta_{\mathsf{r}}^{\mathsf{a}}}{2}\right]$ fall within the receiver main-lobe in the azimuth. Since the strong interferers are assumed to be uniformly and isotropically distributed in $\mathcal{B}\left(\mathsf{R}_0^{\mathcal{P}}, r_{\mathsf{B}}(\mathsf{R}_0^{\mathcal{P}})\right)$, the probability that a strong interferer falls within azimuth beam-width of the reference receiver is $\frac{\theta_{\mathsf{r}}^{\mathsf{a}}}{2\pi}$. Due to the non-isotropy of $\hat{\mathcal{P}} = \mathcal{P} \setminus \mathcal{B}\left(\mathsf{R}_0^{\mathcal{P}}, r_{\mathsf{B}}(\mathsf{R}_0^{\mathcal{P}})\right)$ with respect to the reference receiver, the probability that a weak interferer lies in the receiver main-lobe in the azimuth needs to be computed numerically (using the definition in (27)) and evaluates to $\frac{|\Upsilon(\phi_0^{\mathsf{a}})|}{|\hat{\mathcal{P}}|}$.

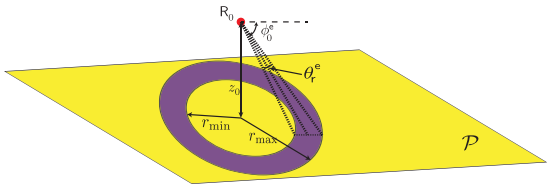

FIGURE 20. Illustration showing the region in $\mathcal{P}$ that falls within the receiver main-lobe due to the elevation beam-width of the antenna.

The region in $\mathcal{P}$ falling within the elevation beam-width of R_0 depends not only on the receiver antenna beam-width $\theta_{\mathsf{r}}^{\mathsf{e}}$ but also on z_0. This is illustrated in Fig. 20.

The region in $\mathcal{B}\left(\mathsf{R}_0^{\mathcal{P}}, r_{\mathsf{B}}(\mathsf{R}_0^{\mathcal{P}})\right)$ that falls within the elevation beam-width of R_0 is an annulus with inner radius $r_{\min}$ and outer radius $\min\left(r_{\mathsf{B}}(\mathsf{R}_0^{\mathcal{P}}), r_{\max}\right)$. The ratio of area of this annulus to the area of $\mathcal{B}\left(\mathsf{R}_0^{\mathcal{P}}, r_{\mathsf{B}}(\mathsf{R}_0^{\mathcal{P}})\right)$ gives the probability that a strong interferer lies within the receiver antenna elevation beam-width. This evaluates to

$$\left(\frac{\min\left(r_{\mathsf{B}}(\mathsf{R}_0^{\mathcal{P}}), r_{\max}\right)^2 - r_{\min}^2}{r_{\mathsf{B}}^2(\mathsf{R}_0^{\mathcal{P}})}\right). \tag{39}$$

Similarly, the probability of being within the elevation beam-width of R_0 for weak interferers is computed as

$$\left(1 - \frac{|\mathcal{P} \setminus \mathcal{B}\left(\mathsf{R}_0^{\mathcal{P}}, \max(r_{\mathsf{B}}(\mathsf{R}_0^{\mathcal{P}}), r_{\max})\right)|}{|\mathcal{P} \setminus \mathcal{B}\left(\mathsf{R}_0^{\mathcal{P}}, r_{\mathsf{B}}(\mathsf{R}_0^{\mathcal{P}})\right)|}\right). \tag{40}$$

Finally, an interferer lies within the main-lobe of the reference receiver if its position in $\mathcal{P}$ falls within both the azimuth and the elevation beam-widths of $\mathsf{R}_0^{\mathcal{P}}$. This leads to the expressions for $p_{\text{rx}}^{\mathsf{SI}}$ and $p_{\text{rx}}^{\mathsf{WI}}$ given in Lemma 2.

APPENDIX C
PROOF OF THEOREM 1

Suppose there are J number of strong interferers. Clearly, J is Poisson distributed with mean $\lambda|\mathcal{B}\left(\mathsf{R}_0^{\mathcal{P}}, r_{\mathsf{B}}(\mathsf{R}_0^{\mathcal{P}})\right)| = \lambda\pi r_{\mathsf{B}}^2(\mathsf{R}_0^{\mathcal{P}})$. With $\ell = \{\ell(\mathsf{R}_0, \mathsf{T}_i)\}_{i=1}^J$, $h = \{h_i\}_{i=1}^J$, $\tilde{G}_{\mathsf{t}} = \left\{G_{\mathsf{t},i}\right\}_{i=1}^J$ and $\tilde{G}_{\mathsf{r}} = \left\{G_{\mathsf{r},i}\right\}_{i=1}^J$,

$$\mathbb{E}_{\Phi}\left[e^{-km\tilde{m}\tilde{\gamma}I_{\Phi}^{\mathsf{SI}}}\right] = \mathbb{E}_J\left[\mathbb{E}_{\ell,h,\tilde{G}_{\mathsf{t}},\tilde{G}_{\mathsf{r}}}\left[\prod_{i=1}^{J} e^{-km\tilde{m}\tilde{\gamma}h_i\ell(\mathsf{R}_0,\mathsf{T}_i)G_{\mathsf{t},i}G_{\mathsf{r},i}}\right]\right].$$

Since h are independent normalized gamma random variables, their moment generating functions can be used to evaluate the expectation with respect to h which leads to

$$\mathbb{E}_J\left[\mathbb{E}_{\ell,\tilde{G}_{\mathsf{t}},\tilde{G}_{\mathsf{r}}}\left[\prod_{i=1}^{J}\left(1 + k\tilde{m}\tilde{\gamma}\,\ell(\mathsf{R}_0, \mathsf{T}_i)G_{\mathsf{t},i}G_{\mathsf{r},i}\right)^{-m}\right]\right]. \tag{41}$$

For strong interferers, $\ell(\mathsf{R}_0, \mathsf{T}_i) = \frac{\|\mathsf{R}_0 - \mathsf{T}_i\|^{-\alpha_{\mathsf{L}}}}{\mathsf{B}_{\mathsf{L}}^{\delta}}$, and $\{\mathsf{T}_i\}_{i=1}^J$ are uniformly and independently distributed in $\mathcal{B}\left(\mathsf{R}_0^{\mathcal{P}}, r_{\mathsf{B}}(\mathsf{R}_0^{\mathcal{P}})\right)$. The expectation with respect to ℓ can be evaluated in two steps - taking an expectation over the number

$$\mathbb{E}_J\left[\mathbb{E}_{\tilde{G}_\mathsf{t}}\left[p_0\left(p_{\mathrm{rx}}^{\mathsf{SI}}\mathcal{F}(G_\mathsf{r},0)+(1-p_{\mathrm{rx}}^{\mathsf{SI}})\mathcal{F}(g_\mathsf{r},0)\right)+\frac{p_1}{2}\left(p_{\mathrm{rx}}^{\mathsf{SI}}\mathcal{F}(G_\mathsf{r},1)+(1-p_{\mathrm{rx}}^{\mathsf{SI}})\mathcal{F}(g_\mathsf{r},1)\right)+\frac{p_1}{2}\mathcal{F}(g_\mathsf{r},1)+p_2\mathcal{F}(g_\mathsf{r},2)\right]^J\right] \tag{44}$$

$$\mathbb{E}_J\left[p_0\sum_{j=1}^{4}\mu_j\left(1-\frac{2}{r_\mathsf{B}^2(\mathsf{R}_0^{\mathcal{P}})}A_{j,0}\right)+\frac{p_1}{2}\sum_{j=1}^{4}\mu_j\left(1-\frac{2}{r_\mathsf{B}^2(\mathsf{R}_0^{\mathcal{P}})}A_{j,1}\right)+\frac{p_1}{2\left(1-p_{\mathrm{rx}}^{\mathsf{SI}}\right)}\sum_{j=3}^{4}\mu_j\left(1-\frac{2}{r_\mathsf{B}^2(\mathsf{R}_0^{\mathcal{P}})}A_{j,1}\right)+\frac{p_2}{\left(1-p_{\mathrm{rx}}^{\mathsf{SI}}\right)}\sum_{j=3}^{4}\mu_j\left(1-\frac{2}{r_\mathsf{B}^2(\mathsf{R}_0^{\mathcal{P}})}A_{j,2}\right)\right]^J \tag{45}$$

of self body blockages s followed by averaging over $r_i=|\mathsf{R}_0^{\mathcal{P}}-\mathsf{T}_i|$ that has distribution

$$f_{r_i}(r)=\tfrac{2r}{r_\mathsf{B}^2(\mathsf{R}_0^{\mathcal{P}})}\ 0\le r\le r_\mathsf{B}(\mathsf{R}_0^{\mathcal{P}}). \tag{42}$$

Using this observation and the distribution in (42), the expectation (41) with respect to ℓ evaluates to

$$\mathbb{E}_J\left[\mathbb{E}_{\tilde{G}_\mathsf{t},\tilde{G}_\mathsf{r}}\left[\prod_{i=1}^{J}\sum_{s=0}^{2}p_s\int_0^{r_\mathsf{B}(\mathsf{R}_0^{\mathcal{P}})}\times\left(1+\frac{k\tilde{m}\tilde{\gamma}G_{\mathsf{r},i}G_{\mathsf{t},i}}{\left(r^2+z_0^2\right)^{\frac{\alpha_\mathsf{L}}{2}}\mathsf{B}_\mathsf{L}^s}\right)^{-m}\frac{2r}{r_\mathsf{B}^2(\mathsf{R}_0^{\mathcal{P}})}\mathrm{d}r\right]\right]. \tag{43}$$

The reference receiver's antenna is pointed towards the reference transmitter, which by our assumption is not blocked by the reference user's body. This implies that the interference from all the strong interferers that fall in $\mathcal{BC}(\mathsf{B}_0)$ signals see a receiver gain of g_r at R_0. The receiver gain at R_0 for the strong interferers outside $\mathcal{BC}(\mathsf{B}_0)$ is either G_r with probability $p_{\mathrm{rx}}^{\mathsf{SI}}$ or g_r with probability $1-p_{\mathrm{rx}}^{\mathsf{SI}}$. Using this observation and the notation,

$$\mathcal{F}(a,s)=\int_0^{r_\mathsf{B}(\mathsf{R}_0^{\mathcal{P}})}\left(1+\frac{k\tilde{m}\tilde{\gamma}aG_{\mathsf{t},i}}{\left(r^2+z_0^2\right)^{\frac{\alpha_\mathsf{L}}{2}}\mathsf{B}_\mathsf{L}^s}\right)^{-m}\frac{2r}{r_\mathsf{B}^2(\mathsf{R}_0^{\mathcal{P}})}\mathrm{d}r,$$

the expectation with respect to $\tilde{G}_\mathsf{r}$ in (43) evaluates to the expression shown in (44), shown at the top of this page. Averaging over the random distribution of $\tilde{G}_\mathsf{t}$, (44) results in (45) which uses the notation in (32). Finally, taking the expectation in (45), shown at the top of this page with respect to Poisson distributed J results in the expression in (33).

APPENDIX D
PROOF OF THEOREM 2

We use the notations $\ell=\{\ell(\mathsf{R}_0,\mathsf{T}_i)\}_{i=1}^K$, $h=\{h_i\}_{i=1}^K$, $\tilde{G}_\mathsf{t}=\left\{G_{\mathsf{t},i}\right\}_{i=1}^K$ and $\tilde{G}_\mathsf{r}=\left\{G_{\mathsf{r},i}\right\}_{i=1}^K$. For simplicity, we use q to denote $q(\mathsf{R}_0,\psi_0)$ here. Noting that the number of weak interferers K is a Poisson distributed random variable with mean $\lambda|\hat{\mathcal{P}}|$, we have $\mathbb{E}_\Phi\left[e^{-km\tilde{m}\tilde{\gamma}I_\Phi^{\mathsf{WI}}}\right]$

$$=\mathbb{E}_K\left[\mathbb{E}_{\ell,h,\tilde{G}_\mathsf{t},\tilde{G}_\mathsf{r}}\left[\prod_{i=1}^{K}e^{-km\tilde{m}\tilde{\gamma}h_i\ell(\mathsf{R}_0,\mathsf{T}_i)G_{\mathsf{t},i}G_{\mathsf{r},i}}\right]\right] \tag{46}$$

$$=\mathbb{E}_K\left[\mathbb{E}_{\tilde{G}_\mathsf{r},\ell}\left[\prod_{i=1}^{K}\left(p_\mathsf{M}\left(1+k\tilde{m}\tilde{\gamma}\,\ell(\mathsf{R}_0,\mathsf{T}_i)G_\mathsf{t}G_{\mathsf{r},i}\right)^{-m}+(1-p_\mathsf{M})\left(1+k\tilde{m}\tilde{\gamma}\,\ell(\mathsf{R}_0,\mathsf{T}_i)g_\mathsf{t}G_{\mathsf{r},i}\right)^{-m}\right)\right]\right], \tag{47}$$

where we used the IID property of h and $\tilde{G}_\mathsf{t}$. Given K, $\{\mathsf{T}_i\}_{i=1}^K$ are uniformly distributed in $\hat{\mathcal{P}}$ and the probability of self-blockage is as per Lemma 1. Using the notations

$$\mathcal{D}(a,b)=\frac{1}{|\hat{\mathcal{P}}|}\int_{z\in\hat{\mathcal{P}}}\left(1+\frac{k\tilde{m}\tilde{\gamma}aG_{\mathsf{r},i}}{b}\right)^{-m}\mathrm{d}z, \tag{48}$$

$$b_1=\|\mathsf{R}_0-z\|_c^{\alpha_\mathsf{L}}\ \text{and} \tag{49}$$

$$b_2=\|\mathsf{R}_0-z\|^{\alpha_\mathsf{N}}, \tag{50}$$

the expectation of (47) with respect to ℓ can be evaluated to give

$$\mathbb{E}_K\mathbb{E}_{\tilde{G}_\mathsf{r}}\left[\prod_{i=1}^{K}\left(q\left[p_\mathsf{M}\mathcal{D}(G_\mathsf{t},b_1)+(1-p_\mathsf{M})\mathcal{D}(g_\mathsf{t},b_1)\right]+(1-q)\left[p_\mathsf{M}\mathcal{D}(G_\mathsf{t},b_2)+(1-p_\mathsf{M})\mathcal{D}(g_\mathsf{t},b_2)\right]\right)\right]. \tag{51}$$

This follows directly using the path-loss model as defined in (15). The orientation of the reference receiver's antenna is such that the interferers falling in $\mathcal{BC}(\mathsf{B}_0)$ always see the side-lobe gain. Using this fact, with $p_{\mathrm{rx}}^{\mathsf{WI}}$ defined in Lemma 2 and with the notations in (30), (31), we can evaluate the expectation with respect to $\tilde{G}_\mathsf{r}$ to simplify (51) as

$$\mathbb{E}_K\left[\frac{q}{|\hat{\mathcal{P}}|}\left(|\hat{\mathcal{P}}|-C_1\right)+\frac{1-q}{|\hat{\mathcal{P}}|}\left(|\hat{\mathcal{P}}|-C_2\right)\right]^K. \tag{52}$$

Taking the expectation of (52) with respect to Poisson distributed K leads to the expressions in Theorem 2.

REFERENCES

[1] IDC. (Jun. 2015). *Worldwide Quarterly Wearable Tracker*. [Online]. Available: https://www.idc.com/tracker/showproductinfo.jsp?prod_id=962

[2] (May 2015). *Wearable Technology 2015–2025: Technologies, Markets, Forecasts*. [Online]. Available: http://www.idtechex.com/research/reports/wearable-technology-2015-2025-%technologies-markets-forecasts-000427.asp

[3] D. Cypher, N. Chevrollier, N. Montavont, and N. Golmie, "Prevailing over wires in healthcare environments: Benefits and challenges," *IEEE Commun. Mag.*, vol. 44, no. 4, pp. 56–63, Apr. 2006.

[4] R. Kohno, K. Hamaguchi, H. B. Li, and K. Takizawa, "R&D and standardization of body area network (BAN) for medical healthcare," in *Proc. IEEE Int. Conf. Ultra-Wideband*, vol. 3. Sep. 2008, pp. 5–8.

[5] D. B. Smith, D. Miniutti, T. A. Lamahewa, and L. W. Hanlen, "Propagation models for body-area networks: A survey and new outlook," *IEEE Antennas Propag. Mag.*, vol. 55, no. 5, pp. 97–117, Oct. 2013.

[6] (Jan. 2008). *IEEE 802.15 WPAN Task Group 6 Body Area Networks*. [Online]. Available: http://www.ieee802.org/15/pub/TG6.html

[7] J. Foerster, J. Lansford, J. Laskar, T. S. Rappaport, and S. Kato, "Realizing Gbps wireless personal area networks—Guest editorial," *IEEE J. Sel. Areas Commun.*, vol. 27, no. 8, pp. 1313–1317, Oct. 2009.

[8] C. Park and T. S. Rappaport, "Short-range wireless communications for next-generation networks: UWB, 60 GHz millimeter-wave WPAN, and ZigBee," *IEEE Wireless Commun.*, vol. 14, no. 4, pp. 70–78, Aug. 2007.

[9] (May 2010). *WirelessHD Specification Version 1.1 Overview*. [Online]. Available: http://www.wirelesshd.org/pdfs/WirelessHD-Specification-Overview-v1.1May2010.pdf

[10] E. Perahia, C. Cordeiro, M. Park, and L. L. Yang, "IEEE 802.11ad: Defining the next generation multi-Gbps Wi-Fi," in *Proc. 7th IEEE Consum. Commun. Netw. Conf.*, Jan. 2010, pp. 1–5.

[11] *2014 Public Transportation Fact Book*, American Public Transportation Association, Nov. 2014.

[12] A. Pyattaev, K. Johnsson, S. Andreev, and Y. Koucheryavy, "Communication challenges in high-density deployments of wearable wireless devices," *IEEE Wireless Commun.*, vol. 22, no. 1, pp. 12–18, Feb. 2015.

[13] S. L. Cotton, W. G. Scanlon, and P. S. Hall, "A simulated study of co-channel inter-BAN interference at 2.45 GHz and 60 GHz," in *Proc. Eur. Wireless Technol. Conf. (EuWIT)*, Sep. 2010, pp. 61–64.

[14] G. George and A. Lozano, "Impact of reflections in enclosed mmWave wearable networks," in *Proc. IEEE Int. Workshop Comput. Adv. Multi-Sensor Adapt. Process. (CAMSAP)*, Dec. 2015, pp. 201–204.

[15] *IEEE Standard for Safety Levels With Respect to Human Exposure to Radio Frequency Electromagnetic Fields, 3 kHz to 300 GHz*, IEEE Standard C95.1-2005, Apr. 2006, pp. 1–238.

[16] T. Wu, T. S. Rappaport, and C. M. Collins, "Safe for generations to come: Considerations of safety for millimeter waves in wireless communications," *IEEE Microw. Mag.*, vol. 16, no. 2, pp. 65–84, Mar. 2015.

[17] K. L. Ryan, J. A. D'Andrea, J. R. Jauchem, and P. A. Mason, "Radio frequency radiation of millimeter wave length: Potential occupational safety issues relating to surface heating," *Health Phys.*, vol. 78, no. 2, pp. 170–181, 2000.

[18] A. Hajimiri, "mm-wave silicon ICs: Challenges and opportunities," in *Proc. IEEE Custom Integr. Circuits Conf. (CICC)*, Sep. 2007, pp. 741–747.

[19] T. S. Rappaport, J. N. Murdock, and F. Gutierrez, Jr., "State of the art in 60-GHz integrated circuits and systems for wireless communications," *Proc. IEEE*, vol. 99, no. 8, pp. 1390–1436, Aug. 2011.

[20] J. Wang *et al.*, "Beam codebook based beamforming protocol for multi-Gbps millimeter-wave WPAN systems," *IEEE J. Sel. Areas Commun.*, vol. 27, no. 8, pp. 1390–1399, Oct. 2009.

[21] (Jan. 2013). *Wilocity Bringing WiGig to Your Desk, Lap, Home and Office*. [Online]. Available: http://http://www.anandtech.com/show/6646/wilocity-bringing-wigig-to-yo%ur-desk-lap-home-and-office

[22] A. Alkhateeb, J. Mo, N. Gonzalez-Prelcic, and R. W. Heath, Jr., "MIMO precoding and combining solutions for millimeter-wave systems," *IEEE Commun. Mag.*, vol. 52, no. 12, pp. 122–131, Dec. 2014.

[23] R. Méndez-Rial, C. Rusu, N. González-Prelcic, A. Alkhateeb, and R. W. Heath, Jr., "Hybrid MIMO architectures for millimeter wave communications: Phase shifters or switches?" *IEEE Access*, vol. 4, pp. 247–267, Jan. 2016, doi: 10.1109/ACCESS.2015.2514261.

[24] J. Brady, N. Behdad, and A. Sayeed, "Discrete lens array modeling and design for optimum MIMO communications at mm-wave," in *Proc. IEEE Antennas Propag. Soc. Int. Symp. (APSURSI)*, Jul. 2012, pp. 1–2.

[25] R. C. Daniels, J. N. Murdock, T. S. Rappaport, and R. W. Heath, Jr., "60 GHz wireless: Up close and personal," *IEEE Microw. Mag.*, vol. 11, no. 7, pp. 44–50, Dec. 2010.

[26] W. Roh *et al.*, "Millimeter-wave beamforming as an enabling technology for 5G cellular communications: Theoretical feasibility and prototype results," *IEEE Commun. Mag.*, vol. 52, no. 2, pp. 106–113, Feb. 2014.

[27] *IEEE 802.15 WPAN Millimeter Wave Alternative PHY Task Group 3c (TG3c)*, accessed on Nov. 2015. [Online]. Available: http://www.ieee802.org/15/pub/TG3c_contributions.html

[28] P. F. M. Smulders and A. G. Wagemans, "Wide-band measurements of MM-wave indoor radio channels," in *Proc. 3rd IEEE Int. Symp. Pers., Indoor Mobile Radio Commun. (PIMRC)*, Oct. 1992, pp. 329–333.

[29] A. Kato, T. Manabe, Y. Miura, K. Sato, and T. Ihara, "Measurements of millimeter wave indoor propagation and high-speed digital transmission characteristics at 60 GHz," in *Proc. Int. Symp. Pers., Indoor Mobile Radio Commun. (PIMRC)*, vol. 1. Sep. 1997, pp. 149–154.

[30] S. Geng and P. Vainikainen, "Millimeter-wave propagation in indoor corridors," *IEEE Antennas Wireless Propag. Lett.*, vol. 8, pp. 1242–1245, Dec. 2009.

[31] G. R. MacCartney, T. S. Rappaport, S. Sun, and S. Deng, "Indoor office wideband millimeter-wave propagation measurements and channel models at 28 and 73 GHz for ultra-dense 5G wireless networks," *IEEE Access*, vol. 3, pp. 2388–2424, Oct. 2015, doi: 10.1109/ACCESS.2015.2486778.

[32] K. Venugopal, M. C. Valenti, and R. W. Heath, Jr., "Interference in finite-sized highly dense millimeter wave networks," in *Proc. IEEE Inf. Theory Appl. Workshop (ITA)*, Feb. 2015, pp. 175–180.

[33] Z. Genc, U. H. Rizvi, E. Onur, and I. Niemegeers, "Robust 60 GHz indoor connectivity: Is it possible with reflections ?" in *Proc. IEEE Veh. Techol. Conf. (VTC)*, May 2010, pp. 1–5.

[34] K. Venugopal, M. C. Valenti, and R. W. Heath, Jr. (Sep. 2015). "Device-to-Device Millimeter Wave Communications: Interference, coverage, rate, and finite topologies." [Online]. Available: http://arxiv.org/abs/1506.07158

[35] F. Baccelli and B. Błaszczyszyn, "Stochastic geometry and wireless networks," in *Foundations and Trends in Networking*. Norwell, MA, USA: NOW Publishers, 2010.

[36] M. Haenggi and R. K. Ganti, *Interference in Large Wireless Networks*. Norwell, MA, USA: NOW Publishers: NOW Publishers, 2009.

[37] J. G. Andrews, R. K. Ganti, M. Haenggi, N. Jindal, and S. Weber, "A primer on spatial modeling and analysis in wireless networks," *IEEE Commun. Mag.*, vol. 48, no. 11, pp. 156–163, Nov. 2010.

[38] T. Bai, A. Alkhateeb, and R. W. Heath, Jr., "Coverage and capacity of millimeter-wave cellular networks," *IEEE Commun. Mag.*, vol. 52, no. 9, pp. 70–77, Sep. 2014.

[39] T. Bai and R. W. Heath, Jr., "Analysis of self-body blocking effects in millimeter wave cellular networks," in *Proc. 48th Asilomar Conf. Signals, Syst. Comput.*, Nov. 2014, pp. 1921–1925.

[40] T. Bai and R. W. Heath, Jr., "Coverage and rate analysis for millimeter-wave cellular networks," *IEEE Trans. Wireless Commun.*, vol. 14, no. 2, pp. 1100–1114, Feb. 2015.

[41] S. Collonge, G. Zaharia, and G. E. Zein, "Influence of the human activity on wide-band characteristics of the 60 GHz indoor radio channel," *IEEE Trans. Wireless Commun.*, vol. 3, no. 6, pp. 2396–2406, Nov. 2004.

[42] J. S. Lu, D. Steinbach, P. Cabrol, and P. Pietraski "Modeling human blockers in millimeter wave radio links," *ZTE Commun.*, vol. 10, pp. 23–28, Dec. 2012.

[43] P. Karadimas, B. Allen, and P. Smith, "Human body shadowing characterization for 60-GHz indoor short-range wireless links," *IEEE Antennas Wireless Propag. Lett.*, vol. 12, pp. 1650–1653, Dec. 2013.

[44] D. Torrieri and M. C. Valenti, "The outage probability of a finite ad hoc network in Nakagami fading," *IEEE Trans. Commun.*, vol. 60, no. 11, pp. 3509–3518, Nov. 2012.

[45] M. C. Valenti, D. Torrieri, and S. Talarico, "Adjacent-channel interference in frequency-hopping ad hoc networks," in *Proc. IEEE Int. Conf. Commun. (ICC)*, Jun. 2013, pp. 5583–5588.

[46] *Railway Passenger Vehicle Capacity: An Overview of the Way Railway Vehicle Capacity Has Evolved*, accessed on Jan. 2015. [Online]. Available: http://www.railway-technical.com/Infopaper%202%20Railway%20Passenger%20%Vehicle%20Capacity%20v1.pdf

[47] K. Venugopal, M. C. Valenti, and R. W. Heath, Jr., "Analysis of millimeter wave networked wearables in crowded environments," in *Proc. Asilomar Conf. Signals, Syst., Comput.*, Nov. 2015, pp. 1–5.

[48] A. Abouraddy and S. Elnoubi, "Statistical modeling of the indoor radio channel at 10 GHz through propagation measurements—Part I: Narrowband measurements and modeling," *IEEE Trans. Veh. Technol.*, vol. 49, no. 5, pp. 1491–1507, Sep. 2000.

[49] D. Beauvarlet and K. L. Virga, "Measured characteristics of 30-GHz indoor propagation channels with low-profile directional antennas," *IEEE Antennas Wireless Propag. Lett.*, vol. 1, no. 1, pp. 87–90, Feb. 2005.

[50] H. Alzer, "On some inequalities for the incomplete gamma function," *Math. Comput.*, vol. 66, pp. 771–778, Apr. 1997.

KIRAN VENUGOPAL received the B.Tech. degree in electronics and communication engineering from the National Institute of Technology, Calicut, in 2011, and the M.E. degree in telecommunication engineering from the Indian Institute of Science, Bangalore, in 2013. He received the Prof. S. V. C. Aiya Medal for best M.E. (Telecommunications) student from the Indian Institute of Science, Bangalore, 2013, and the Er. M.L. Bapna Gold Medal for scoring the highest CGPA among all the under graduate programs from the National Institute of Technology, Calicut, in 2011. From 2013 to 2014, he was a Systems Design Staff Engineer with Broadcom Communication Technologies Pvt. Ltd., Bangalore, where he primarily dealt with the physical layer design and implementation aspects of WiFi modems. He is currently pursuing the Ph.D. degree with the Wireless Networking and Communications Group, Department of Electrical and Computer Engineering, The University of Texas at Austin. In summer 2015, he was a Graduate Intern with Intel Labs, Santa Clara. His research interests include wireless communication, signal processing, network coding, and estimation theory.

ROBERT W. HEATH, JR. (S'96–M'01–SM'06–F'11) received the B.S. and M.S. degrees from the University of Virginia, Charlottesville, VA, in 1996 and 1997, respectively, and the Ph.D. degree from Stanford University, Stanford, CA, in 2002, all in electrical engineering. From 1998 to 2001, he was a Senior Member of the Technical Staff and then a Senior Consultant with Iospan Wireless Inc., San Jose, CA, where he worked on the design and implementation of the physical and link layers of the first commercial MIMO-OFDM communication system. Since 2002, he has been with the Department of Electrical and Computer Engineering, The University of Texas at Austin, where he is a Cullen Trust for Higher Education Endowed Professor, and is a member of the Wireless Networking and Communications Group. He is also the President and CEO of MIMO Wireless Inc. and the Chief Innovation Officer of Kuma Signals LLC. His research interests include several aspects of wireless communication and signal processing: limited feedback techniques, multihop networking, multiuser and multicell MIMO, interference alignment, adaptive video transmission, manifold signal processing, and millimeter wave communication techniques. He has co-authored the book entitled *Millimeter Wave Wireless Communications* (Prentice Hall, 2014).

He has been an Editor of the IEEE TRANSACTIONS ON COMMUNICATION, an Associate Editor of the IEEE TRANSACTIONS ON VEHICULAR TECHNOLOGY, and a Lead Guest Editor of the IEEE JOURNAL ON SELECTED AREAS IN COMMUNICATIONS of the Special Issue on Limited Feedback Communication, and the IEEE JOURNAL ON SELECTED TOPICS IN SIGNAL PROCESSING of the Special Issue on Heterogenous Networks. He was on the Steering Committee of the IEEE TRANSACTIONS ON WIRELESS COMMUNICATIONS from 2011 to 2014. He was a member of the Signal Processing for Communications Technical Committee in the IEEE Signal Processing Society and was the Chair of the IEEE COMSOC Communications Technical Theory Committee. He was a Technical Co-Chair of the 2007 Fall Vehicular Technology Conference, the General Chair of the 2008 Communication Theory Workshop, the General Co-Chair, Technical Co-Chair, and Co-Organizer of the 2009 IEEE Signal Processing for Wireless Communications Workshop, the Local Co-Organizer of the 2009 IEEE CAMSAP Conference, the Technical Co-Chair of the 2010 IEEE International Symposium on Information Theory, the Technical Chair of the 2011 Asilomar Conference on Signals, Systems, and Computers, the General Chair of the 2013 Asilomar Conference on Signals, Systems, and Computers, the Founding General Co-Chair of the 2013 IEEE GlobalSIP Conference, and the Technical Co-Chair of the 2014 IEEE GLOBECOM Conference.

Dr. Heath was a co-author of best student paper awards at the IEEE VTC 2006 Spring, WPMC 2006, the IEEE GLOBECOM 2006, the IEEE VTC 2007 Spring, and the IEEE RWS 2009, and a co-recipient of the Grand Prize in the 2008 WinTech WinCool Demo Contest. He was a co-recipient of the 2010 and 2013 *EURASIP Journal on Wireless Communications and Networking* best paper awards, the 2012 *Signal Processing Magazine* best paper award, a 2013 Signal Processing Society Best Paper Award, the 2014 *EURASIP Journal on Advances in Signal Processing* Best Paper Award, and the 2014 *Journal of Communications and Networks* Best Paper Award. He was a 2003 Frontiers in Education New Faculty Fellow. He is also a Licensed Amateur Radio Operator and is a Registered Professional Engineer in Texas.